Monthly Notices
of the
ROYAL ASTRONOMICAL SOCIETY

MNRAS **504,** 3203–3220 (2021)
Advance Access publication 2021 April 27

doi:10.1093/mnras/stab822

NGC 6611 601: a hot pre-main-sequence spectroscopic binary containing a centrifugal magnetosphere host star

M. E. Shultz,[1]★ E. Alecian,[2] V. Petit ,[1] S. Bagnulo,[3] T. Böhm,[4,5] C. P. Folsom,[5,6] G. A. Wade[6] and the MiMeS Collaboration

[1]*Department of Physics and Astronomy, University of Delaware, 217 Sharp Lab, Newark, DE 19716, USA*
[2]*IPAG, Université Grenoble Alpes, F-38000 Grenoble, France*
[3]*Armagh Observatory and Planetarium, College Hill, Armagh BT61 9DG, Northern Ireland, UK*
[4]*IRAP, Université de Toulouse, CNRS, CNES, UPS, F-31400 Toulouse, France*
[5]*IRAP, CNRS, 14 avenue Edouard Belin, F-31400 Toulouse, France*
[6]*Department of Physics and Space Science, Royal Military College of Canada, Kingston, ON K7K 7B4, Canada*

Accepted 2021 March 16. Received 2021 March 16; in original form 2020 October 3

ABSTRACT

W 601 (NGC 6611 601) is one of the handful of known magnetic Herbig Ae/Be stars. We report the analysis of a large data set of high-resolution spectropolarimetry. The star is a previously unreported spectroscopic binary, consisting of two B2 stars with a mass ratio of 1.8, masses of 12 and 6.2 $M_{\odot}$, in an eccentric 110-d orbit. The magnetic field belongs to the secondary, W 601 B. The H α emission is consistent with an origin in W 601 B's centrifugal magnetosphere; the star is therefore not a classical Herbig Be star in the sense that its emission is not formed in an accretion disc. However, the low value of $\log g = 3.8$ determined via spectroscopic analysis and the star's membership in the young NGC 6611 cluster are most consistent with it being on the pre-main sequence. The rotational period inferred from the variability of the H α line and the longitudinal magnetic field $\langle B_z \rangle$ is 1.13 d. Modelling of Stokes V and $\langle B_z \rangle$ indicates a surface dipolar magnetic field $B_{\rm d}$ between 6 and 11 kG. With its strong emission, rapid rotation, and strong surface magnetic field, W 601 B is likely a precursor to H α-bright magnetic B-type stars such as σ Ori E. By contrast, the primary is an apparently non-magnetic ($B_{\rm d} < 300$ G) pre-main-sequence early B-type star. In accordance with expectations from magnetic braking, the non-magnetic primary is apparently more rapidly rotating than the magnetic star.

Key words: stars: early-type – stars: individual: NGC 6611 601 – stars: magnetic field – stars: massive – stars: rotation.

1 INTRODUCTION

Approximately 10 per cent of main-sequence (MS) and pre-main-sequence (PMS) stars with radiative envelopes host strong (∼kG scale), organized (predominantly dipolar) magnetic fields (Grunhut et al. 2017; Sikora et al. 2019a). Since radiative envelopes cannot support a contemporaneous convective dynamo, it is believed that the magnetic fields of early-type stars are fossils – remnants from a previous stage in the stars' evolution (e.g. Braithwaite & Spruit 2004; Neiner et al. 2015). Consistent with the fossil field hypothesis is that, unlike dynamo magnetic fields, hot star magnetic fields are apparently stable over a time span of at least decades (e.g. Shultz et al. 2018b), show no general correlation between magnetic field strength and rotational properties, and exhibit a decline in surface magnetic field strength over evolutionary time-scales consistent with conservation or slow decay of magnetic flux (e.g. Landstreet et al. 2007, 2008; Shultz et al. 2019d; Sikora et al. 2019b).

The origin of fossil magnetic fields remains obscure. One scenario is that they arise due to short-lived dynamos generated during binary mergers (e.g. Schneider et al. 2019); however, this is difficult to reconcile with the orbital properties of known close magnetic binary systems such as the doubly magnetic system ϵ Lupi (Shultz et al. 2015b), the tidally locked system HD 98088 (Folsom et al. 2013), the very close binary HD 156324 (Shultz et al. 2018a), or the 'identical twins' of HD 62658 (Shultz et al. 2019e). A competing scenario is that fossil fields may be remnants of convective dynamos operating on the PMS (e.g. Mestel 1999), in which case the 10 per cent incidence ratio might perhaps be explained by a PMS dynamo bistability mechanism similar to that seen in fully convective stars (as discussed by Shultz et al. 2019e) combined with rapid rotationally or convectively driven decay of magnetic fields failing to reach critical surface strength (Aurière et al. 2007; Jermyn & Cantiello 2020).

This makes examination of magnetic hot stars on the PMS a key arena for determining the origin of fossil magnetic fields. Only eight PMS early-type stars with magnetic field detections confirmed with high-resolution spectropolarimetry are known (Wade et al. 2005; Catala et al. 2007; Alecian et al. 2008a, b, 2013a; Petit et al. 2008; Hubrig et al. 2009, 2013, 2015; Järvinen et al. 2015). Alecian et al. (2013a, b) showed that fossil magnetic fields have the same incidence among Herbig Ae/Be stars as among the MS population, and tend to be more slowly rotating than non-magnetic Herbig stars, which is consistent with the magnetic stars being subject to magnetic

★ E-mail: mshultz@udel.edu

braking. A spectropolarimetric survey of intermediate-mass T Tauri stars by Villebrun et al. (2019) demonstrated that magnetic fields are ubiquitous among stars with convective envelopes, but that the incidence declines to around 10 per cent immediately upon crossing the boundary on the Hertzsprung–Russell diagram (HRD) between convective and radiative envelopes.

Since only a few magnetic PMS hot stars are known, a full magnetic and rotational characterization of the individual members of this population is an important step in understanding their properties. In this paper, we examine the PMS B2 star NGC 6611 601 (also known as NGC 6611−019, ALS 9522, BD −13° 4937, and hereafter referred to as W 601). This star was classified as a Herbig Ae/Be star on the basis of its 'P-Cygni like' Hα emission (Martayan et al. 2008) and its mid-infrared excess (Kumar et al. 2004). Its magnetic field was detected by Alecian et al. (2008b), who also noted its strong, variable He lines, suggesting that it may be a He-strong star. W 601 is an X-ray source (Nazé et al. 2014) and a radio synchrotron source (Kurapati et al. 2017), both likely indicative that the star hosts a detectable magnetosphere; the other possible explanation for enhanced X-rays and non-thermal radio emission – colliding winds – seems unlikely due to the relatively weak winds of B-type stars, and unnecessary due to the presence of a magnetic field.

The observations – a large ESPaDOnS data set – are described in Section 2. In Section 3, we show the evidence that W 601 is a spectroscopic binary, and constrain the orbital properties of the system. Stellar parameters are revisited in the light of binarity in Section 4. The magnetic analysis is presented in Section 5, where it is determined that the magnetic field belongs to the secondary. Spectroscopic variability is examined in Section 6, and in Section 7 the rotational period is determined from the magnetic and spectroscopic variations. The magnetic properties of the stars are derived in Section 8. The magnetospheric properties of the system, and its possible future magnetic and rotational evolution, are discussed in Section 9, along with implications for the origins of fossil magnetic fields, their accompanying chemical abundance anomalies, and the status of the system as a Herbig star. Conclusions are summarized in Section 10.

2 OBSERVATIONS

The data set consists of 27 spectropolarimetric ESPaDOnS sequences obtained at the 3.6-m Canada–France–Hawaii Telescope (CFHT) from several observing programmes (programme codes 06BF15, 07AF06, 08AF16, 08AC13, 08BP14, 12AP13, and 13BC09), and in the context of the Magnetism in Massive Stars (MiMeS) Large Program. ESPaDOnS is a fibre-fed echelle spectropolarimeter with a spectral resolution $\lambda/\Delta\lambda \sim 65\,000$ at 500 nm, and a wavelength coverage between about 370 and 1050 nm. Each observation consists of four polarized sub-exposures, which are combined to yield a circular polarization (Stokes *V*) spectrum and two diagnostic null *N* spectra, with which anomalies in instrument behaviour can be detected. The reduction and analysis of ESPaDOnS data was described in detail by Wade et al. (2016). The data were reduced with the Libre-ESPRIT pipeline (Donati et al. 1997).

The observation log is given in Table 1. The mean peak signal-to-noise (S/N) per spectral pixel is about 200.

Four of these observations were already reported by Alecian et al. (2008b) (one on 2006 August 10, two on 2007 March 6, and one on 2007 March 9). The remaining observations are presented here for the first time.

3 BINARITY

Magnetic Bp stars exhibit several forms of line profile variation. The first, and most common in this class, are due to inhomogeneous surface chemical abundance patches, almost invariably exhibiting different patterns of variation for different elements (e.g. Kochukhov et al. 2015; Rusomarov et al. 2015, 2016; Silvester et al. 2017; Rusomarov, Kochukhov & Lundin 2018; Kochukhov, Shultz & Neiner 2019). Many Bp stars also exhibit line profile variability due to pulsation or binarity. As is shown below, the line profile variations of W 601 reported by Alecian et al. (2008b), and interpreted there as the signature of He spots, are in fact primarily due to binarity.

Close examination of the line profile variability shows that lines of different elements exhibit essentially the same pattern of variation (Fig. 1), with absorption excesses appearing in the same part of the line regardless of element. Since it is not expected that different elements will display the same abundance distributions, the similarity of the line profile variability between lines from different elements suggests that the source of the variation may instead be either binarity or pulsation.

To test the binarity hypothesis, two-component models were fit to the strong He I 667.8 nm line using the parametrized line profile fitting routine described by Grunhut et al. (2017). This process yielded consistent fits for a broad-lined component ($v \sin i = 173 \pm 14$ km s^{-1}) and a narrow-lined component ($v \sin i = 105 \pm 3$ km s^{-1}), where the uncertainties are determined from the standard deviation of fits across the data set. The RVs of the two components obtained in the course of profile fitting anticorrelate with one another (Fig. 2, top). Since the broad-lined component has the smaller RV amplitude, we designate it as the primary, W 601 A, and the narrow-lined component as W 601 B. W 601 A has an RV semi-amplitude of about 20 km s^{-1} and W 601 B has a semi-amplitude of about 30 km s^{-1}. There is no detectable RV variation on a time-scale of 1 to 2 d, however, there is significant variation over a time-scale of weeks. This is in contrast to EW variations tracing rotational variability, which occur on a much shorter time-scale (see Section 6).

The RVs and $v \sin i$ values were then used to disentangle the line profiles of various spectral lines using the iterative method described by González & Levato (2006), as shown for the He I 667.8 nm, Si III 455.3 nm, and Si II 634.7 nm lines in Fig. 1. As can be seen in Fig. 1, the broad-lined component accounts for the majority of line absorption: 57 per cent of the absorption in He I 667.8 nm, 74 per cent in Si III 455.3 nm, and 63 per cent in Si II 634.7 nm.

The anticorrelation of the RVs, and the fact that the larger RV amplitude is seen in the component with the smaller contribution to the line absorption, are all consistent with W 601 being a double-lined spectroscopic binary (SB2).

Period analyses of the RVs were performed using both the standard Fourier analysis package PERIOD04[1] (Lenz & Breger 2005) and using the IDL routine PERIODOGRAM.PRO[2] (Horne & Baliunas 1986). Period uncertainties were determined analytically (Bloomfield 1976). Analysis of the full RV data set yielded ambiguous results, with numerous peaks of similar amplitude between about 30 and 200 d. Since there is only minimal variation on time-scales of a few days (Fig. 2, left-hand panel), we analysed mean weekly RVs in order to avoid biasing the periodogram results by the few highly sampled epochs. This strategy yielded a period of 109.9(2) d from both the A and B RVs (see Fig. 3, where periodograms from PERIODOGRAM.PRO are shown).

[1] Available at https://www.univie.ac.at/tops/Period04/.
[2] Available at https://hesperia.gsfc.nasa.gov/ssw/gen/idl/util/periodogram.pro.

Table 1. Observation log, radial velocity (RV) measurements, and $\langle B_z \rangle$ measurements. S/N indicates the maximum signal-to-noise per spectral pixel in the ESPaDOnS spectrum. Average RV uncertainties are 1.8 km s^{-1} for W 601 A and 1.5 km s^{-1} for W 601 B. DF refers to the magnetic field detection flag (DD: definite detection; MD: marginal detection; ND: non-detection).

Date	HJD −2453000	S/N	RV_A (km s^{-1})	RV_B (km s^{-1})	$\langle B_z \rangle$ (G)	DF_V	$\langle N_z \rangle$ (G)	DF_N
10/08/2006	957.76004	220	5	20	184 ± 286	DD	−139 ± 286	ND
02/03/2007	1162.15478	103	−7	38	−709 ± 1015	ND	−1067 ± 1015	ND
03/03/2007	1163.12053	192	0	31	408 ± 348	ND	−644 ± 348	ND
04/03/2007	1164.12133	226	−2	34	−857 ± 286	ND	−391 ± 286	ND
05/03/2007	1165.13840	254	−6	41	−805 ± 247	ND	−450 ± 247	ND
06/03/2007	1166.10187	179	−6	45	−511 ± 343	ND	116 ± 343	ND
06/03/2007	1166.14879	153	−7	47	−458 ± 617	ND	213 ± 617	ND
07/03/2007	1167.11236	182	−9	49	−117 ± 362	MD	59 ± 362	ND
08/03/2007	1168.10114	194	−6	45	1424 ± 354	DD	−508 ± 354	ND
08/03/2007	1168.14652	204	−9	47	921 ± 332	DD	606 ± 332	ND
09/03/2007	1169.10634	190	0	38	2014 ± 349	DD	−813 ± 348	ND
09/03/2007	1169.15224	199	−1	36	2036 ± 370	DD	−246 ± 369	ND
30/06/2008	1647.80106	203	35	−30	2095 ± 311	DD	547 ± 311	ND
30/06/2008	1647.84933	191	35	−30	2079 ± 335	DD	336 ± 334	ND
30/06/2008	1647.89851	185	33	−28	1784 ± 354	DD	31 ± 354	ND
30/06/2008	1647.94664	175	31	−25	1797 ± 393	DD	−589 ± 392	ND
30/06/2008	1647.99560	179	28	−19	443 ± 359	MD	−283 ± 359	ND
30/06/2008	1648.04373	179	29	−19	1178 ± 382	DD	−33 ± 382	ND
01/07/2008	1648.80655	209	31	−30	1446 ± 311	DD	200 ± 310	ND
01/07/2008	1648.85518	205	31	−26	1808 ± 325	DD	17 ± 324	ND
01/07/2008	1648.90492	202	32	−28	2509 ± 327	DD	−499 ± 326	ND
01/07/2008	1648.95328	205	31	−25	2359 ± 320	DD	−212 ± 320	ND
01/07/2008	1649.00232	219	33	−28	2053 ± 291	DD	6 ± 290	ND
01/07/2008	1649.05057	213	31	−25	1748 ± 299	DD	101 ± 299	ND
29/07/2008	1676.89812	167	9	15	370 ± 412	ND	−430 ± 412	ND
21/06/2012	3099.93880	272	24	−8	2088 ± 308	DD	−170 ± 307	ND
13/08/2013	3517.80010	264	34	−27	1256 ± 329	DD	480 ± 329	ND

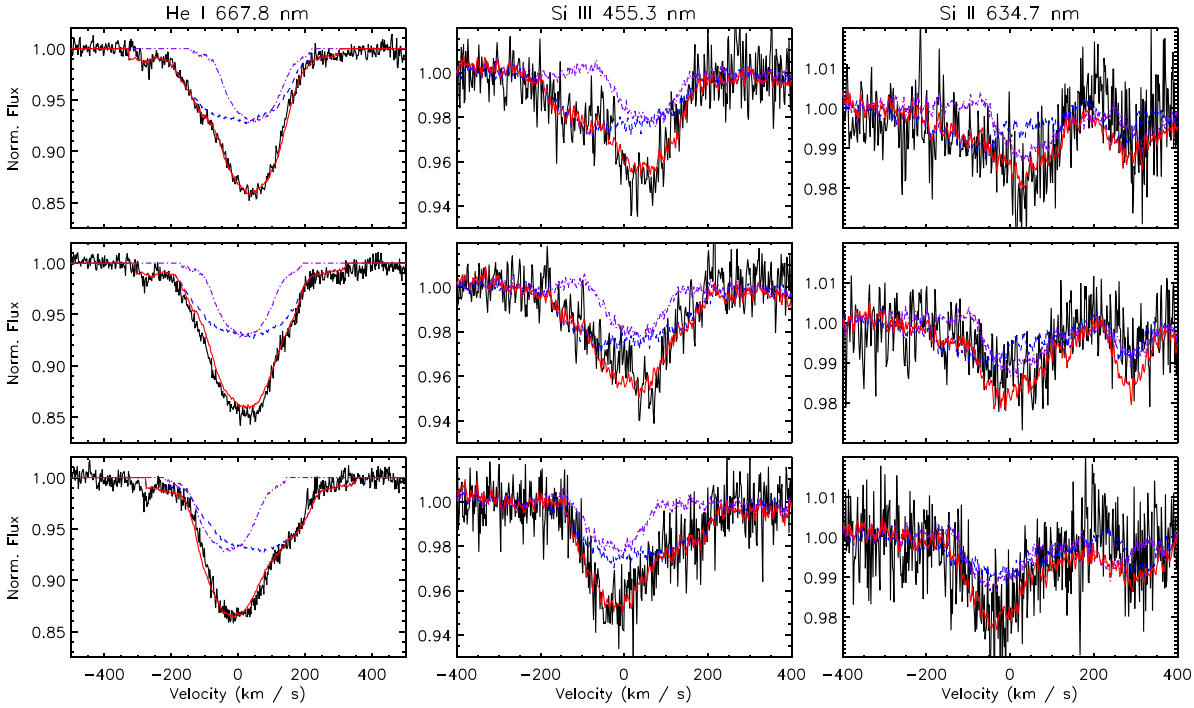

Figure 1. Observed line profiles (black lines) and disentangled line profiles (dashed blue: primary; dot–dashed purple: secondary; solid red: cumulative) for three isolated spectral lines. Each row shows the same spectrum. The top, middle, and bottom rows, respectively, show spectra with the secondary at maximum positive RV, the minimum difference in RV between primary and secondary, and with the secondary at maximum negative RV. Line profile variations in all lines can be reproduced assuming a two-star model with variable RVs.

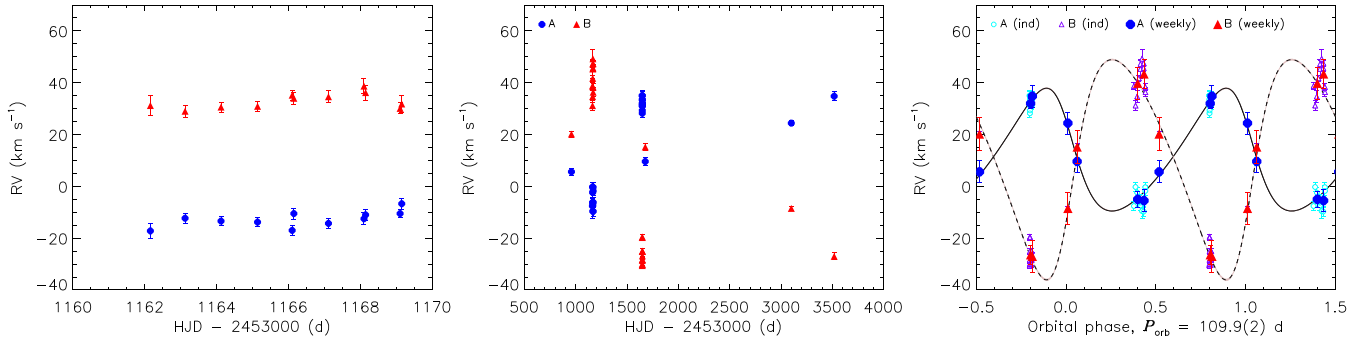

Figure 2. RVs for the primary (blue circles) and secondary (red triangles) as a function of time (left, middle) and phased with the orbital period (right). The left-hand panel zooms in on the epoch with the densest time sampling. In the right-hand panel, curves and shaded regions indicate orbital models and uncertainties.

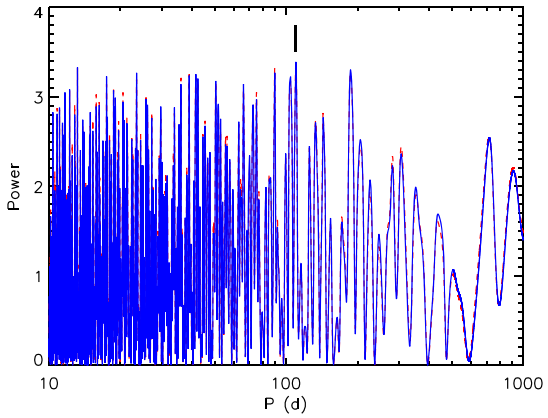

Figure 3. Periodograms for the primary (solid blue) and secondary (dashed red) mean weekly RVs. The thick black line indicates the maximum power period. Note that there are several peaks of nearly equivalent significance; these are discussed further in the text.

PERIOD04 instead yielded a period of 104 d, however, the longer period obtained using PERIODOGRAM.PRO provides a better phasing of the data (Fig. 2, right). The longer period furthermore yields a higher S/N as evaluated using PERIOD04 itself (26 as compared to 5.5). We therefore adopt the period from PERIODOGRAM.PRO as the most likely orbital period, although we note that there is enough ambiguity in the period that it should certainly be tested by further observation.

To obtain an orbital solution, we optimized synthetic RV curves against the mean weekly RVs using a Markov chain Monte Carlo algorithm (as described by Shultz et al. 2018a, 2019a). The algorithm achieved rapid convergence, providing additional confidence in the period. The model fits to the RVs are shown in the right-hand panel of Fig. 2, and the fit parameters are given in Table 2. The orbit is mildly eccentric ($e = 0.24 \pm 0.01$), with a mass ratio $M_A/M_B = 1.79 \pm 0.04$. The χ^2 of the fit shown in Fig. 2 is 3.6. MCMC fitting of the 104 d period yielded a χ^2 of 15.4, with a noticeably worse fit. The periodogram also has a peak at 186 d, nearly the same strength as the 109 d period; fitting with this period yielded a χ^2 of 6.7, somewhat higher than the 109 d period. This indicates that the 109 d period is the most likely to be correct. Notably, while the three fits yield different eccentricities e and velocity semi-amplitudes K, the systemic velocities v_0 and the mass ratios $M_A/M_B = K_B/K_A$ are essentially identical in all three cases, indicating that these parameters are likely robust against future revision of the orbital period.

Table 2. Orbital parameters: orbital period P_{orb}; epoch of periastron T_0; eccentricity e; argument of periastron ω; central velocity v_0; semi-amplitudes K_A and K_B; mass ratio M_A/M_B; projected total mass $M\sin^3 i$; projected component masses $M_A \sin^3 i$ and $M_B \sin^3 i$; and projected semimajor axis $a \sin i$.

Parameter	Value	Uncertainty
P_{orb} (d)	109.9	0.2
T_0 (HJD)	2453900.8	0.2
e	0.234	0.008
ω (°)	64.6	0.9
v_0 (km s^{-1})	11.4	0.1
K_A (km s^{-1})	21.5	0.2
K_B (km s^{-1})	41.8	0.4
M_A/M_B	1.94	0.03
$M\sin^3 i$ ($M_\odot$)	2.64	0.06
$M_A \sin^3 i$ ($M_\odot$)	1.75	0.04
$M_B \sin^3 i$ ($M_\odot$)	0.90	0.02
$a \sin i$ (au)	0.621	0.005

4 STELLAR PARAMETERS

Stellar parameters for W 601 have previously been determined by de Winter et al. (1997) ($\log L/L_\odot = 4.28$, T_{eff} =23.5 kK) and Dufton et al. (2006) ($\log L/L_\odot = 3.96 \pm 0.11$, T_{eff} =22.4 ± 2.7 kK, and $\log g = 3.85$), where the different luminosities arise from different assumptions regarding distance and extinction. Since these parameters were determined under the assumption of a single star, they need to be revisited.

4.1 Effective temperature

As a first pass to estimate the T_{eff} of the two components, we used EW ratios of Si II 634.7 nm and Si III 455.3 nm obtained from disentangled line profiles (Fig. 1). While surface abundances are by definition affected by the chemical spots expected for a magnetic chemically peculiar star, line strength ratios for different ions of the same element are not affected by this (since it is the abundance, but not the T_{eff}, that varies across the stellar surface; e.g. Shultz et al. 2015a, 2019b). Comparison of the weighted mean EW ratios calculated from all spectra to theoretical values obtained from the NLTE TLUSTY BSTAR2006 library of synthetic spectra (Lanz & Hubeny 2007), using $3.5 < \log g < 4.25$, yields $T_{effA} = 22.5 \pm 1.5$ kK and $T_{effB} = 20.5 \pm 1.5$ kK. While the T_{eff} of the two components

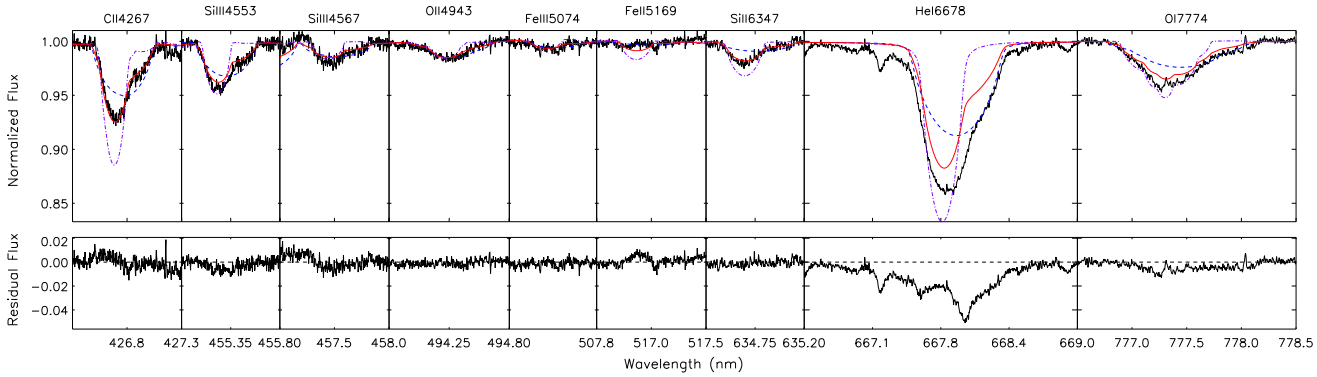

Figure 4. Comparison of the best-fitting composite TLUSTY spectrum (red lines) to the observed mean spectrum obtained via co-addition of observations with similar RVs (black lines). Contributions from the primary (dashed blue) and secondary (dot–dashed purple) show the intrinsic flux from each component, i.e. not scaled by the luminosity ratio. The bottom panel shows the residuals after subtraction of the model. Note the poor fit to He I 667.8 nm, indicative of one of the stars being a He-strong star; this line was not used for parameter determination.

overlaps within uncertainty, B is definitely cooler than A, since the contribution of A is higher in Si III as compared to Si II.

A second analysis is demonstrated in Fig. 4, where we used a grid of synthetic spectra calculated from TLUSTY models, with 15 $< T_{\rm eff} <$ 25 kK and 3.0 $< \log g <$ 4.5 for each star. The TLUSTY spectra were calculated with 2 km s^{-1} of microturbulence and solar metallicity. The radius ratio $R_{\rm A}/R_{\rm B}$ was allowed to vary as a free parameter between 0.5 and 5, where $R_{\rm A}/R_{\rm B}$ is a factor used to scale the contributions of the A and B components to the composite spectrum. $v \sin i_{\rm A} = 173$ km s^{-1}, $v \sin i_{\rm B} = 94$ km s^{-1}, RV$_{\rm A} = 35$ km s^{-1}, and RV$_{\rm B} = -23$ km s^{-1} were fixed. The grid was compared to a mean spectrum created by combining the ESPaDOnS observations obtained in 03/2007, since the RVs of the two components are basically constant during the 1 week of observations (see the left-hand panel of Fig. 2. The standard deviation in RV is 3.5 km s^{-1} and 6 km s^{-1} for W 601 A and B, respectively, in both cases comparable to the uncertainty in $v \sin i$; co-addition of spectra therefore should not lead to significant additional line broadening.), and this is the epoch with the largest number of observations. The peak S/N per 1.8 km s^{-1} spectral pixel of the mean 2007 spectrum is 670. The analysis was performed on a selection of strong lines, shown in Fig. 4, with a focus on chemical species for which two ionization levels are present in the spectrum (O I and II; Si II and III; and Fe II and III). The results of this analysis are $T_{\rm eff,\,A} = 22 \pm 1$ kK, $T_{\rm eff,\,B} = 19 \pm 1$ kK, $\log g = 3.75 \pm 0.25$ for both stars, and $R_{\rm A}/R_{\rm B} = 1.1 \pm 0.1$.

The results of the spectroscopic fit are consistent with those of the EW ratio analysis, but use a larger number of lines, and yield more precise results; we therefore adopt the spectroscopic fit results for the $T_{\rm eff}$. The surface gravity is revisited below using Balmer lines, as these are more sensitive to $\log g$.

Alecian et al. (2008b) classified W 601 as a He-strong star because its He lines were much stronger than solar abundance models predict, as is usually the case for strongly magnetic stars in this $T_{\rm eff}$ regime. As can be seen in Fig. 4, a binary spectroscopic model with solar abundances also results in He lines much weaker than observed. For this reason, He lines were not included in the $T_{\rm eff}$ determination.

4.2 Surface gravity

To refine the determination of $\log g$, we examined the H β and H γ lines. Since there is emission in H α, there will also be (weaker) emission in the higher-numbered H Balmer lines. In order to mitigate

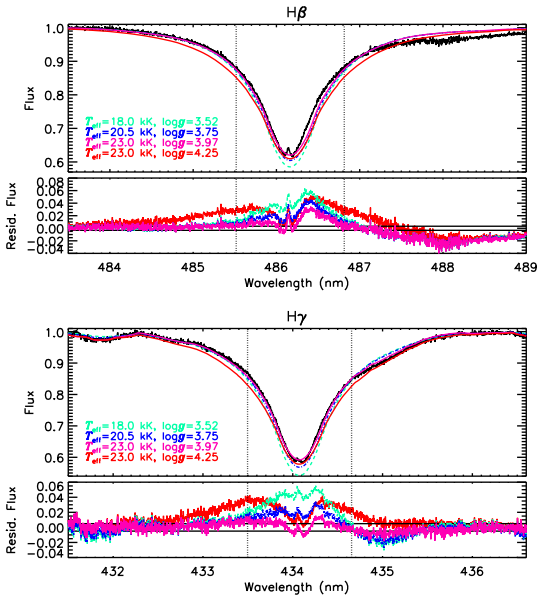

Figure 5. Single component fits to the H β and H γ lines. Vertical dotted lines indicate regions excluded from the fit. Note the flat residuals outside the exclusion regions; residuals inside are due to circumstellar emission. Legends indicate the $T_{\rm eff}$ and $\log g$ of the corresponding models. Bottom sub-panels show the residual flux. Cyan, blue, and purple lines indicate best-fitting values for the given $T_{\rm eff}$; the red line shows $\log g = 4.25$ for comparison. Note the much deeper wings of the $\log g = 4.25$ model in comparison to the observed spectrum.

the influence of this emission on the Balmer wings, a mean spectrum was created from the observations exhibiting the smallest amount of H α emission. The mean spectra were obtained from merged and normalized spectral orders in the same fashion as described by Shultz et al. (2019b). Fits were performed outside of $\pm$200 km s^{-1} i.e. excluding the rotationally broadened core of the primary. While the H α emission can extend out to $\pm$700 km s^{-1}, in the case of the low-emission mean spectrum the significant emission is contained within the $\pm$200 km s^{-1} exclusion range, as can be verified from the residuals in Fig. 5. Rotationally broadened synthetic spectra from the BSTAR2006 library were utilized for the fits, with χ^2 minima being determined for three values of $T_{\rm eff}$ spanning the range of $T_{\rm eff}$ of the primary and secondary. Here, we have made the assumption that

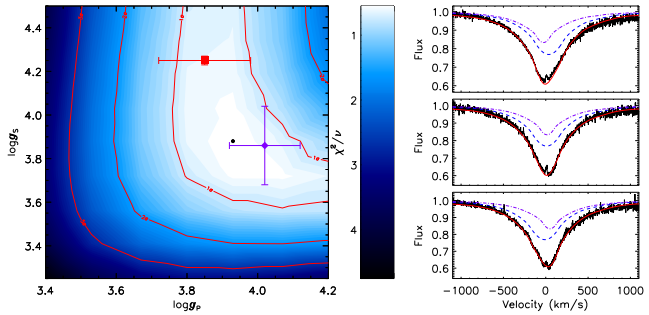

Figure 6. Two-component fit to H β. The left-hand panel shows the χ^2 landscape (range indicated by colour bar), with the best-fitting model parameter indicated with black dots. Red contours indicate σ-levels. The diamond and square, respectively, indicate surface gravities inferred from MS and PMS evolutionary models (Fig. 7). Right-hand panels show the fits to H β, at (top to bottom), maximum primary RV, minimum RV separation, minimum primary RV (observed: black lines; dashed blue lines, primary; dot–dashed purple lines, secondary; solid red lines, combined flux).

a single-star model can yield reasonable results, given both the low amplitude of the RV variation and the similar $T_{\rm eff}$ of the two stars. As can be seen from Fig. 5, H β and H γ return similar values for $\log g$, 3.68 ± 0.22 and 3.75 ± 0.23 (cgs), respectively.

We next performed a two-component fit to H β accounting for the contributions and RV variation of both stars. Here, the same method was adopted as by Shultz et al. (2019b), with the radius of the secondary constrained by the orbital mass ratio and $\log g$. As before, only observations exhibiting minimal emission, confined to the central ± 200 km s^{-1} region of the line, were utilized, and this velocity range was excluded from the fit. The results are shown in Fig. 6, and are consistent with the single-component fit: $\log g_{\rm A} = 3.9^{+0.3}_{-0.1}$, and $\log g_{\rm B} = 3.9^{+0.5}_{-0.3}$.

4.3 Fundamental parameters and evolutionary status

W 601 has been reported as a PMS star (Martayan et al. 2008; Alecian et al. 2008b). As its status as a classical Herbig Ae/Be star is doubtful due to the nature of its H α emission (see Section 6 and Section 7), it is not clear at this stage in the analysis whether the star is on the MS or the pre-MS, since its H α emission does not appear to be from an accretion disc. Here, we seek to determine whether the star is on the PMS or on the MS. The low measured surface gravity is potentially consistent with two scenarios: either the stars are on the PMS, or the primary has evolved towards the terminal age MS (TAMS).

As a first step, it is necessary to know whether or not W 601 is a member of the young NGC 6611 cluster, since if it is a member this establishes an upper limit on the star's age, and additionally gives better constraints on the distance than are available from the *Gaia* parallax of the individual star. Cantat-Gaudin et al. (2018) identified W 601 as a member of NGC 6611 with an 80 per cent probability using *Gaia* DR2 parallaxes and proper motions (Gaia Collaboration 2018). The star's DR2 parallax and proper motions are furthermore below the 3 and 5σ rejection thresholds used by Kuhn et al. (2019) to determine cluster membership (respectively, differing by about 2.3σ and 2.8σ from the mean cluster values, using the smaller cluster uncertainty). The *Gaia* early Data Release 3 parallax and proper motions of W 601 are furthermore identical within uncertainty to the mean cluster values determined by Kuhn et al. (2019) on the basis of *Gaia* DR2 values. W 601's systemic velocity, $v_0 = 11.4 \pm 0.2$ km s^{-1}, is also consistent with the mean cluster RV of 10 ± 8 km s^{-1} determined from the VLT-FLAMES survey by Evans et al. (2005). We conclude that W 601 is very likely to be a member of NGC 6611.

The mean *Gaia* parallax of the cluster is $\pi_{\rm cl} = 0.57 \pm 0.04$ mas, corresponding to a distance of $d = 1740^{+130}_{-120}$ pc (Kuhn et al. 2019). From isochrone fitting of the MS turnoff, the NGC 6611 cluster is between 0 and 6 Myr in age according to de Winter et al. (1997), while Dufton et al. (2006) found an age of 3 ± 1 Myr using VLT-FLAMES data. Hillenbrand et al. (1993) found ages of 0.25 Myr to 1 Myr for young stellar objects (YSOs) below 8 M$_\odot$, and determined an average age of 2 ± 1 Myr for stars above 9 M$_\odot$. Getman et al. (2018) found the cluster's YSOs to be between 1 and 2.6 Myr. All studies seem to agree that the oldest stars in the cluster are no more than 6 Myr in age, and that the cluster also contains ongoing star formation.

Measurements of extinction in NGC 6611 are widely variable across the region, ranging from $A_{\rm V} = 1.7$ to 7.2 (e.g. Dufton et al. 2006; Guarcello et al. 2007; Maíz Apellániz & Barbá 2018). There is furthermore evidence of a non-standard reddening law of between $R_{\rm V} = 3.5$ and 3.9 (e.g. Hillenbrand et al. 1993; Kumar et al. 2004; Guarcello et al. 2007; Maíz Apellániz & Barbá 2018). To constrain the extinction and reddening of W 601, we utilized the star's *UBVJHK* photometry (Høg et al. 2000; Cutri et al. 2003; Wolff et al. 2007), and de-reddened these using the IDL program FM_UNRED.PRO (Fitzpatrick & Massa 1999), with reddening $0 < E(B-V) < 1$ and reddening law $3 < R_{\rm V} < 5$. The dereddened colours $U-B$, $B-V$, $V-J$, $V-H$, and $V-K$ were then compared to the intrinsic colours from the empirical PMS calibration determined by Pecaut & Mamajek (2013). The best match was obtained for $E(B-V) = 0.55$ and $R_{\rm V} = 4.37$, yielding $A_{\rm V} = 2.39$. The reddening law is steeper than obtained for other stars in the cluster, however, fixing $R_{\rm V} = 3.5$ yields $E(B-V) = 0.68$, with $A_{\rm V}$ almost unchanged. These results are consistent with those obtained by previous examinations of the star (e.g. Kumar et al. 2004; Dufton et al. 2006).

In order to constrain the luminosity and the other fundamental stellar parameters, the binary Monte Carlo (MC) HRD sampler described by Pablo et al. (2019) was utilized. This algorithm takes as priors the photometric properties of the system (V magnitude, extinction, parallax), the orbital mass ratio (Table 2), and the individual effective temperatures and surface gravities, and infers the luminosities, masses, ages, and radii via interpolation through evolutionary models under the assumption that the two components are coeval (but not interacting) (Bonnell & Bate 1994). Bolometric corrections for both stars were obtained from the calibration of Nieva (2013). The $T_{\rm eff} - \log g$ diagram is sampled with points drawn from Gaussian distributions matching $T_{\rm eff}$ and $\log g$ values of the two stars, and are probabilistically rejected if the inferred mass ratio, absolute V mag, and age differ from target values drawn from Gaussian distributions with standard deviations set respectively by the measured uncertainty in the mass ratio, the combined uncertainty in distance modulus and extinction, and an arbitrary tolerance in $\log t$. The results are shown in Fig. 7, and the parameters are given in Table 3.

We determined stellar parameters using two sets of evolutionary models, the rotating MS models published by Ekström et al. (2012) (i.e. those with an initial rotation velocity of 0.4 of the critical value; bottom panels of Fig. 7), and the rotating PMS models developed by Haemmerlé et al. (2019) (top panels of Fig. 7), both of them calculated using the Geneva 1D stellar evolution code. The MS models start at the zero-age main sequence (ZAMS), whereas the PMS models start at the birthline. For the PMS models, an age tolerance of $\log t = 0.15$ was adopted for the MC sampling, in order to reflect the possibility that very young stars might not be perfectly

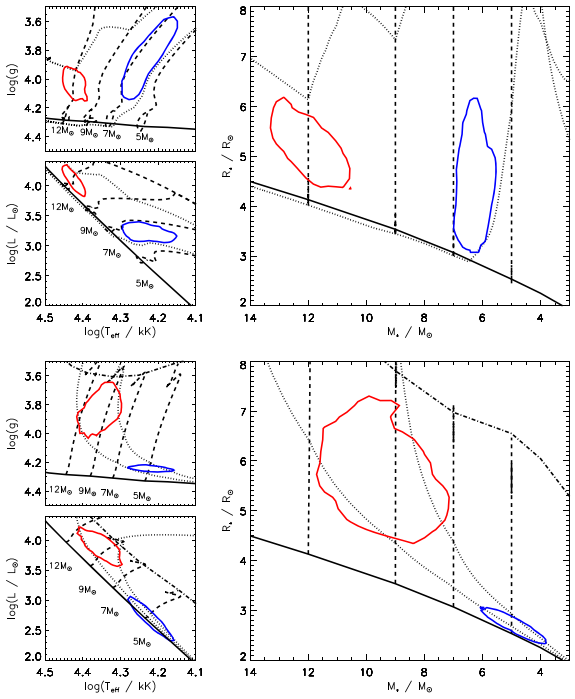

Figure 7. Stellar parameters inferred from MC sampling of the HRD using pre-MS models (Haemmerlé et al. 2019, top panels) and MS models (Ekström et al. 2012, bottom panels). Contours show 1σ uncertainties (red: primary; blue: secondary). The solid line shows the ZAMS; dashed and dotted lines, respectively, show evolutionary tracks and isochrones. For the PMS models, isochrones are shown for $\log t = 5.4$ and 5.7; for the MS models, isochrones for $\log t = 7.1$ and 7.5 are shown. A comparison between the $\log g$ values determined from evolutionary models to those measured via spectroscopic modelling is shown in Fig. 6.

coeval; for the MS models a tolerance of 0.05 was used, ensuring any accepted points would lie on the same isochrone.

PMS models yield an age of $\log(t/\mathrm{yr}) = 5.6 \pm 0.1$, while the MS models yield an age of $\log t = 7.3 \pm 0.2$. Only the age derived from PMS evolutionary models is consistent with the 6 Myr ($\log t = 6.8$) upper limit on the cluster age.

The MS models predict that W 601 A has a larger radius than W 601 B, whereas the PMS models yield similar radii (compare the top and bottom right panels of Fig. 7). The ratio of radii from PMS MC parameter determination ($R_\mathrm{A}/R_\mathrm{B} = 1.2 \pm 0.3$) is consistent with results from spectral modelling ($R_\mathrm{A}/R_\mathrm{B} = 1.1 \pm 0.1$). Using MS models, the radii ratio is $R_\mathrm{A}/R_\mathrm{B} = 2.1 \pm 0.3$, which is not consistent with the spectroscopy.

While the MC sampler initially draws from distributions in $\log g$ and T_eff as determined from spectroscopic measurements, due to the various rejection criteria the posterior distributions of $\log g$ do not necessarily resemble the input distributions. MS models can only maintain coevality if $\log g_\mathrm{A} = 3.85 \pm 0.12$ and $\log g_\mathrm{S} = 4.24 \pm 0.02$, i.e. if the primary has evolved about halfway towards the TAMS, the secondary should still be very close to the ZAMS. Conversely, PMS models yield $\log g_\mathrm{A} = 4.06 \pm 0.10$ and $\log g_\mathrm{B} = 3.86 \pm 0.18$. A comparison to the spectroscopic measurement of $\log g$ is provided on the χ^2 map in Fig. 6. Both the MS and PMS results are consistent with the best-fitting value within the 1σ contours, although the PMS results are closest to the χ^2 minima.

PMS models yield a better match to the measured surface gravities, radius ratio, and the age of the NGC 6611 cluster. We therefore conclude that the scenario with the greatest consistency is that both components of W 601 are still contracting towards the ZAMS. It is additionally notable that the Hα line displays nebular emission (Section 6), suggesting the system is still partially embedded in the nebula.

Table 3. Stellar parameters for the W 601 components.

Parameter	A	B
B (mag)	11.11	
V (mag)	10.78	
d (kpc) [a]	1.74 ± 0.13	
$E(B-V)$	0.68 ± 0.05	
A_V (mag) [b]	2.38 ± 0.3	
M_V (mag)	-3.0 ± 0.4	-1.7 ± 0.3
BC (mag) [c]	-2.6 ± 0.1	-1.6 ± 0.2
M_bol (mag)	-5.7 ± 0.4	-3.3 ± 0.3
T_eff (kK)	22 ± 1	19 ± 1
$\log g$ (cm s^{-1})	$3.9^{+0.3}_{-0.1}$	$3.9^{+0.5}_{-0.3}$
$\log(L/\mathrm{L}_\odot)$	4.1 ± 0.2	3.2 ± 0.1
R_* ($\mathrm{R}_\odot$)	5.2 ± 0.7	4.3 ± 0.9
M_* ($\mathrm{M}_\odot$)	12 ± 1	6.2 ± 0.4
$\log(t/\mathrm{yr})$ (PMS)	5.6 ± 0.2	
$\log(t/\mathrm{yr})$ (MS)	7.3 ± 0.2	
i_orb ($^\circ$)	31.5 ± 0.9	
a (au)	1.18 ± 0.02	

[a]Kuhn et al. (2019); [b]using the anomalous extinction law determined by Dufton et al. (2006); [c]Nieva (2013). PMS models: Haemmerlé et al. (2019); MS models: Ekström et al. (2012).

As can be seen in the top panels of Fig. 7, PMS models indicate that the ages of W 601 A and B differ by about $\log t = 0.2$, or about 200 kyr at the inferred age of the system. Reducing the age tolerance does not change this result; in fact an age tolerance of $\log t = 0.15$ is the minimum necessary to keep the rejection rate reasonably small. This may indicate that the two components are not precisely coeval, but that the primary formed before the secondary.

From the stellar masses, the MC parameter analysis additionally yields an orbital inclination $i_\mathrm{orb} = 31.5 \pm 0.9^\circ$ and thus a semimajor axis $a = 1.18 \pm 0.02$ au.

5 MAGNETOMETRY

In order to increase the S/N of the line profile from which the magnetic field is measured, least squares deconvolution (LSD; Donati et al. 1997; Kochukhov, Makaganiuk & Piskunov 2010) profiles were extracted from the ESPaDOnS spectra. We used a line mask obtained with an 'extract stellar' request from the Vienna Atomic Line Database (VALD3; Piskunov et al. 1995; Ryabchikova et al. 1997; Kupka et al. 1999, 2000; Ryabchikova et al. 2015) for a 19 kK solar metallicity star, with $\log g = 3.8$, and a line depth threshold of 0.1. The mask was cleaned in the usual fashion in order to remove contamination from H Balmer, telluric, and interstellar lines (e.g. Shultz et al. 2018b). In addition to the interstellar Ca lines, W 601's spectrum contains several diffuse interstellar bands (DIBs) that were also removed from the line mask. DIBs were identified by eye, including but not necessarily limited to lines with approximate wavelengths of 472 nm, 476 nm, 496 nm, 523 nm, 540 nm, 541 nm, 549 nm, 551 nm, 554 nm, 578 nm, 579 nm, 585 nm, 661 nm, and 666 nm.

Due to the large $v \sin i$ and low S/N of the data, He lines were left in the mask. The resulting LSD profiles were scaled to a line depth of 0.1, a mean wavelength of 500 nm, and a mean Landé factor of 1.2. To further increase the per-pixel S/N, a velocity pixel width of

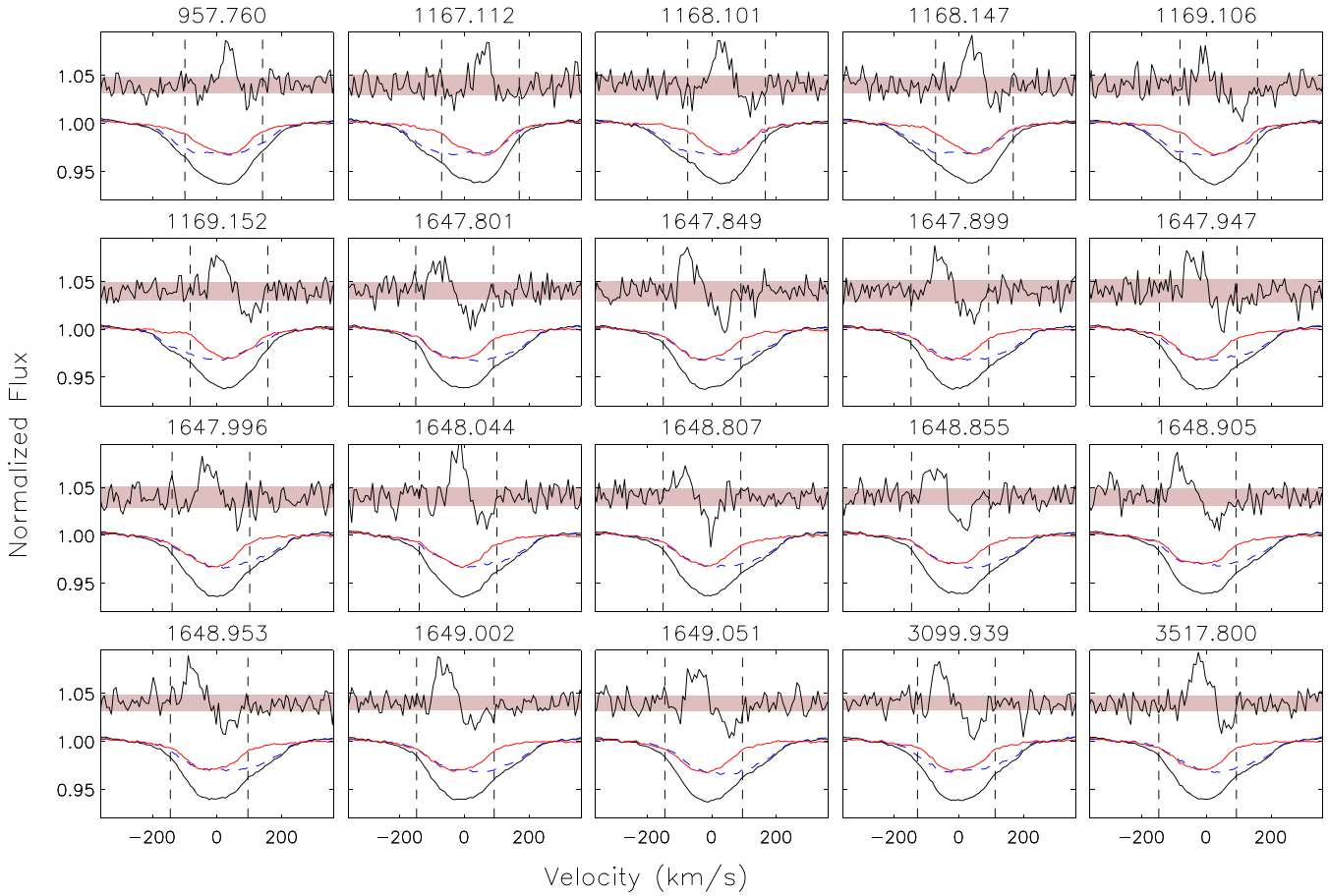

Figure 8. LSD profiles. Each panel is labelled with HJD−2453000. Only LSD profiles yielding at least an MD in Stokes *V* are shown. In each panel, the full Stokes *I* profile is shown with black lines. The disentangled Stokes *I* profiles of W 601 A and B are, respectively, shown with dashed blue and solid red lines. Above Stokes *I* is the Stokes *V* profile. The shaded region indicates the mean uncertainty in Stokes *V*. Vertical dashed lines indicate the integration limits used for measuring the FAP and $\langle B_z \rangle$. Note that Stokes *V* is confined within the line profile of the secondary, and tracks its RV variation. It is therefore the secondary that is the magnetic star.

7.2 km s^{-1} was used. A Tikhonov regularization factor of 0.2 was employed in order to suppress noise arising from the deconvolution process (Kochukhov et al. 2010). Following extraction, the LSD profiles were iteratively disentangled using the same procedure as adopted in Section 3 (e.g. González & Levato 2006). The results are shown in Fig. 8. The Zeeman signature is confined within the line profile of W 601 B, and tracks the RV variation of this component; thus, it is W 601 B that hosts the magnetic field. Further magnetic analysis was therefore conducted using the disentangled Stokes *I* profiles of W 601 B. Since the non-magnetic star only contributes noise to Stokes *V*, flux dilution does not affect magnetic measurements so long as the disentangled spectrum of the magnetic component is used (see e.g. Petit et al. 2019).

Observations were classified as definite, marginal, or non-detections (DD, MD, or ND) according to the False Alarm Probabilities (FAPs) measured inside the line profile, using the method and criteria described by Donati, Semel & Rees (1992) and Donati et al. (1997). The integration ranges used for measuring the FAP are shown in Fig. 8, and detection flags for individual stars are given in Table 1. Of the 27 total observations, 18 yield DDs, 2 MDs, and 7 NDs. FAPs measured from the null *N* spectra are uniformly non-detections.

We measured the strength of the magnetic field via the disc-averaged longitudinal magnetic field (e.g. Mathys 1989; Wade et al. 2000), using the same integration ranges as used for measuring the FAP (i.e. about ±120 km s^{-1} centred on the RV of W 601 B). These measurements, as well as the $\langle N_z \rangle$ measurements obtained from the *N* profiles, are given in Table 1.

While the *N* profiles are all NDs, the $\langle N_z \rangle$ measurements show a systematic bias towards negative values. Close examination revealed that several of the Stokes *V* and *N* continua of several of the observations are offset from the expected value of 0. This may be a consequence of the ratio of continuum flux in the two polarization beams changing as the retarder rotates (Bagnulo et al. 2012), likely exacerbated by the low S/N of the observations. Re-adjusting the continua of the LSD Stokes *V* and *N* profiles to null corrected this issue, yielding $\langle N_z \rangle$ scattered evenly about 0. The amplitude of $\langle B_z \rangle$ was slightly increased, although not outside of the error bars.

$\langle B_z \rangle$ ranges from about −1 to +2 kG, with a mean uncertainty of 360 G. Even without knowing the rotation period or magnetic configuration, the maximum value of $\langle B_z \rangle$ indicates that the surface magnetic dipole strength B_d must be at least 7 kG (under the simplest assumption of a dipolar surface magnetic field, in which case the lower limit on B_d is about 3.5× the maximum value of $\langle B_z \rangle$). Since both positive and negative values of $\langle B_z \rangle$ are measured, both magnetic poles must come into view over the course of a rotational cycle.

6 LINE PROFILE VARIABILITY

W 601 was originally classified as a Herbig Be star on the basis of its youth and Hα emission (Alecian et al. 2008b; Martayan et al. 2008). T Tauri stars and Herbig Ae/Be stars generally show variable emission in multiple lines, not only Hα (Mendigutía et al. 2011a). The morphologies and variability patterns of the line emission of T Tauri stars are explained by the magnetospheric accretion model (Bouvier et al. 2007), in which the inner disc material is locked to and therefore in corotation with the star's magnetic field, leading to the formation of a gap between the photosphere and the inner rim of the disc. Linear Hα spectropolarimetry confirms the existence of this gap in both T Tauri stars and Herbig Ae stars (Vink et al. 2005), and the line emission of at least one magnetic Herbig Ae star is consistent with magnetospheric accretion (Schöller et al. 2016). However, the line emission of early-type Herbig Be stars is generally not consistent with magnetospheric accretion (Mendigutía et al. 2011b; Wichittanakom et al. 2020), which is not surprising given the very low incidence of detected magnetic fields in this population.

The presence of a strong magnetic field and evidently rapid rotation may indicate that W 601 may be the first Herbig Be star with Hα emission consistent with magnetospheric accretion. However, the absence of the expected emission in other lines (Mendigutía et al. 2011a) suggests that the star's Hα profile may instead be consistent with an origin in a wind-fed 'centrifugal magnetosphere' (CM; Landstreet & Borra 1978; Petit et al. 2013), since rapidly rotating, strongly magnetic early B-type stars almost invariably possess CMs detectable in Hα (Shultz et al. 2019d).

Inspection of the Hα line indicates that the morphology of the Hα emission is consistent with a CM, i.e. a double-humped emission profile with the peak emission occurring at velocities equal to several times the projected rotational velocity $v \sin i$, as can be seen in Fig. 9. This shape arises due to rigid corotation of magnetically confined plasma with the photospheric magnetic field, which results in the confined plasma rotating at velocities that increase linearly with distance from the star. Beyond the Kepler corotation radius $R_{\rm K}$, centrifugal support is stronger than gravity and gravitational infall of the confined plasma is prevented (e.g. ud-Doula, Owocki & Townsend 2008). This leads to an accumulation of material above $R_{\rm K}$, and a cavity below $R_{\rm K}$, thereby giving rise to the double-humped morphology (e.g. Townsend & Owocki 2005). A Keplerian disc seen edge-on can also produce a double-humped emission profile, however, the crucial difference with σ Ori E-type emission is that the emission of a Keplerian disc is confined inside $\pm v \sin i$.

To analyse the time variability of Hα, we measured its EWs. We utilized the individual Stokes I spectra in order to maximize the size and time-resolution of the data set (i.e. 108 spectra). EWs were measured in the red half of the line, from $+v \sin i$ to the red edge of emission at $+700$ km s^{-1}, and in the blue half of the line between the blue edge of emission at -700 km s^{-1} and $-v \sin i$. The core of the line was excluded so as to avoid contaminating the measurements with nebular emission (Fig. 9). To correct for the EW variation due to the RV variations of the two components, for each spectrum we calculated synthetic binary spectra in the same fashion as was done for H β in determining $\log g$ (Fig. 6), using the best-fitting parameters for each star and a radius ratio of $R_{\rm A}/R_{\rm B} = 1.1$ as inferred from spectroscopic modelling (Fig. 4). The EWs of the model spectra were measured within the same integration ranges, and subtracted from the EWs of the data. These EWs are used to determine the rotational period below in Section 7.1. Line profile variations are examined in greater detail in the context of the magnetospheric analysis in Section 9.1.

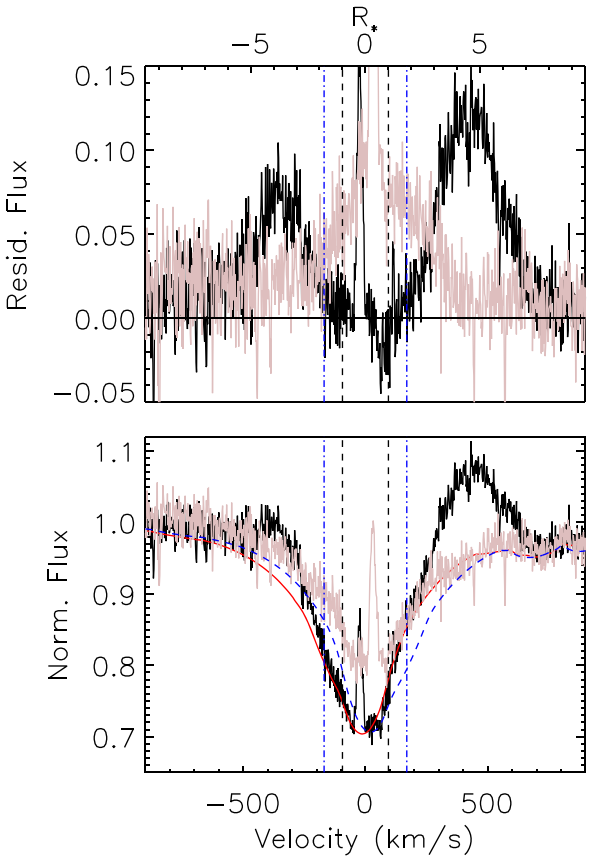

Figure 9. *Bottom*: Hα profiles at minimum emission (grey) and maximum emission (black), with respective synthetic binary profiles (dashed blue, solid red). Dashed black vertical lines indicate $\pm v \sin i$ for W 601 B; dot–dashed blue vertical lines indicate $\pm R_{\rm K}$. The profiles have been shifted to the rest-frame of the secondary. The thin emission feature in the centre of the line is nebular emission. *Top*: Residual flux after subtracting synthetic from observed spectra. The double-humped emission, peaking at several times $v \sin i$, is a characteristic signature of a CM. Note that the top axis is in units of stellar radii, reflecting the assumption that the emission is produced by magnetically confined material in corotation with the star.

Magnetic hot stars typically have surface chemical abundance spots that lead to rotational modulation of EW measurements from photospheric line profiles. We examined the He I 667.8 nm, Si III 455.4 nm, and C II 426.7 nm lines, choosing these lines on the basis of being relatively strong and isolated. The EWs of these lines were measured from individual Stokes I subexposures across the full line width, as inferred by eye, with the individual spectra renormalized using a linear fit to adjacent continuum regions. There is no statistically significant variability in either Si III or C II (the reduced χ^2 for the null assumption of no variation about the mean value being in both cases about unity). He I, however, exhibits statistically significant variation, and this line was also included in the period analysis in Section 7.1.

7 ROTATION

7.1 Period determination

Magnetic hot stars generally exhibit spectropolarimetric and spectroscopic variations modulated precisely by the rotation period, with no inter-cycle variations i.e. the variability is perfectly regular. Therefore, the rotation period can be determined independently using

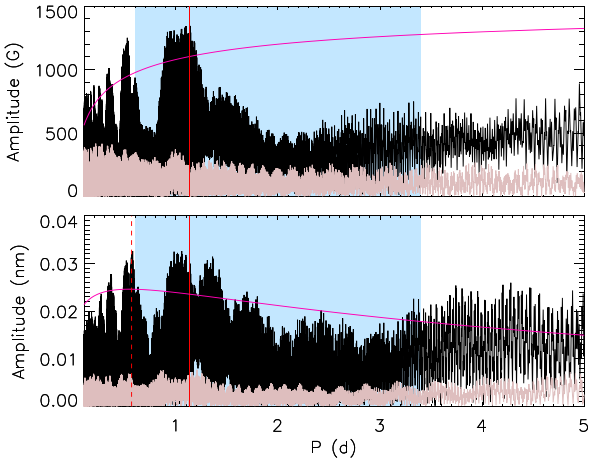

Figure 10. Periodograms for $\langle B_z \rangle$ (top) and Hα EWs (bottom). Shaded regions indicate the physically plausible range of periods (see text). Periodograms are shown in black. The 3σ noise level is shown by purple curves. The adopted rotation period is indicated with a solid red line. For the Hα periodogram, red dashed lines indicate rotational harmonics. Grey periodograms are after pre-whitening with the rotation period (top) or the rotation period and its harmonics (bottom).

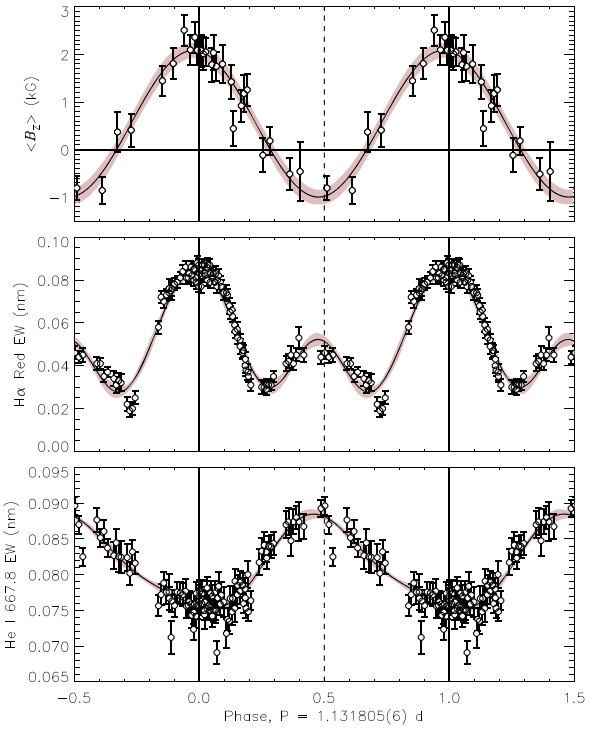

Figure 11. $\langle B_z \rangle$ (top), red Hα emission EW (middle), and He I 667.8 nm EW (bottom), phased with the rotation period. Curves and grey shaded regions show harmonic fits to the data and 1σ uncertainties. Solid and dashed vertical lines indicate magnetic extrema. EWs were obtained from individual Stokes *I* sub-exposures. All data have been sigma-clipped to remove the noisiest observations. Hα emission peaks occur at the extrema of $\langle B_z \rangle$, as expected for rotationally modulated magnetospheric emission.

multiple diagnostics. The period analysis of individual diagnostics ($\langle B_z \rangle$, Hα and He I 667.8 nm EWs) is described in the following, with 1.131805(6) d from Hα EWs being adopted as the most likely rotational period.

As a first attempt to determine the rotation period the $\langle B_z \rangle$ measurements were analysed using PERIOD04. The resulting periodogram is shown in the top panel of Fig. 10. The shaded region indicates the range of physically plausible rotation periods, with the lower bound set by the breakup velocity and the upper bound set by R_* and $v \sin i$. Within this window, the highest peak is at 1.13980(3) d (with the uncertainty in the least significant digit given in parentheses), with an S/N of 9, i.e. the period is above the threshold of 4 usually adopted for formal significance (Breger et al. 1993; Kuschnig et al. 1997). However, there are numerous other nearby peaks with a similar amplitude, and it is not possible to distinguish between them based purely on the coherence of the phase variation.

We also analysed the EWs described in Section 6 using PERIOD04. The Hα periodogram is shown in the bottom panel of Fig. 10. There is a single strong peak at about 1.15 d, consistent with the forest of peaks obtained for $\langle B_z \rangle$. However, the strongest signal is at 0.56589 d, very close to the first harmonic of the period identified in $\langle B_z \rangle$. This is typical of the double-wave EW variations produced by the CMs of stars in which both magnetic poles are visible during a rotation cycle, as is the case with W 601 B (e.g. Landstreet & Borra 1978; Shultz et al. 2020). Under the presumption that this is one-half of the true rotation period, we fit the period and this harmonic with PERIOD04 in order to obtain a period of 1.13179(1) d. The S/N of the rotational period and its first harmonic are, respectively, 7 and 12. If EWs measured from the red half of the line (Section 6) are analysed in isolation – where the emission strength is at a maximum and the amplitude of variation is the largest – the respective S/N of the rotation period and its first harmonic are 27 and 29, with $P_{\rm rot}$ = 1.131805(6) d. Analysing the blue Hα EWs in isolation does not yield useful results. The strongest peak in the periodogram is at about 0.558783(6) d, qualitatively consistent although formally inconsistent with the first harmonic of the period obtained from the red EWs; however, the S/N of this period is not high (5.6). We adopt the period obtained from the red EWs as the most precise, and the most likely to be correct.

For He I 667.8 nm, the strongest peak is at 1.09099(2) d. However, if the He I EWs are phased with the Hα period, PERIOD04 returns a higher amplitude (0.006 nm versus 0.005 nm) and a higher S/N (11.5 versus 9.8). Since Hα yields a higher S/N, the slightly different period returned by He I 667.8 nm is probably a consequence of the lower S/N of the variation of this line (the semi-amplitude of variation in this line being less than 3× the mean error bar).

7.2 Rotational modulation

$\langle B_z \rangle$, Hα EWs, and He I 667.8 nm EWs are shown phased with $P_{\rm rot}$ in Fig. 11, using $JD0 = 2453957.4(2)$ as determined by fitting a sinusoid to $\langle B_z \rangle$ and determining the $\langle B_z \rangle$ maximum one cycle before the first observation. The reduced χ^2 of a first-order sinusoidal fit to $\langle B_z \rangle$ is 1.3, indicating that a sinusoid is a good fit and that $\langle B_z \rangle$ can therefore be reproduced by a simple tilted dipole, as is the case for most magnetic early-type stars (e.g. Shultz et al. 2018b; Kochukhov et al. 2019).

The He I EWs phase coherently with the rotational period (Fig. 11, bottom), with the extrema of the He I EW curve corresponding to the $\langle B_z \rangle$ extrema. The He variability pattern suggests that the strongest He abundance spot is at the negative magnetic pole. Coherent EW variation is notable in the case of a PMS star, as it suggests that surface chemical abundance patches form almost immediately in the photospheres of magnetic hot stars.

Table 4. Rotational, magnetic, and magnetospheric parameters for W 601 B (see text for definitions).

Parameter	Value
$P_{\rm rot}$ (d)	1.13178 ± 0.00001
T_0 (HJD)	2453957.4 ± 0.2
$i_{\rm rot}$ (°)	31^{+5}_{-3}
$v_{\rm eq}$ (kms)	161^{+33}_{-9}
W	$0.24^{+0.09}_{-0.01}$
$R_{\rm p}/R_{\rm e}$	$0.971^{+0.003}_{-0.03}$
$R_{\rm K}$ (R_*)	$2.1^{+0.2}_{-0.2}$
B_0 (kG)	0.54 ± 0.07
B_1 (kG)	1.55 ± 0.09
β (°)	79^{+1}_{-3}
$B_{\rm d}$ (kG)	11^{+3}_{-1}
$\log(\dot{M}/{\rm M}_\odot\,{\rm yr}^{-1})$	-9.5 ± 0.1
v_∞ (km s^{-1})	1120 ± 60
$\log \eta_*$	6.0 ± 0.2
$R_{\rm A}$ (R_*)	31^{+5}_{-2}
$\log R_{\rm A}/R_{\rm K}$	1.2 ± 0.1
$\log(B_{\rm K}/{\rm G})$	2.7 ± 0.2
$\log(\tau_{\rm J}/{\rm yr})$	$6^{+0.3}_{-0.1}$
$\log(t_{\rm S,\,max}/{\rm yr})$	$5.8^{+0.5}_{-0.1}$

The rotational modulation of Hα is examined in detail in Section 9.1.

8 MAGNETIC MODELLING

The rotationally magnetic variability of hot stars is described using the Oblique Rotator Model (ORM; e.g. Stibbs 1950), in which the sinusoidal variation in $\langle B_z \rangle$ of a dipolar magnetic field rotating in the plane of the sky is parametrized with the inclination $i_{\rm rot}$ of the rotational axis from the line of sight, the tilt angle β of the magnetic axis from the rotational axis, and the strength of the magnetic dipole at the stellar surface $B_{\rm d}$.

To determine W 601 B's rotational, ORM, and magnetospheric parameters, we utilized the MC HRD sampler described by Shultz et al. (2019d). The MC sampler combines information about a star's observed atmospheric, magnetic, and rotational properties, together with ancillary information such as e.g. the age of its parent cluster, with evolutionary models in order to infer fundamental stellar parameters, ORM parameters, rotational parameters, and magnetospheric parameters. These are given in Table 4.

As inputs we used the stellar parameters obtained above (Fig. 7, Table 3), the star's rotational period, and $v \sin i$ to obtain $i_{\rm rot} = 31^{\circ+5}_{-3}$. This is similar to the orbital axis inclination $i_{\rm orb} = 31.5 \pm 0.9°$, i.e. the spin and orbital axes of the system are aligned or nearly aligned. The sinusoidal fitting parameters to $\langle B_z \rangle = B_0 + B_1 \sin(\phi + \Phi)$ are $B_0 = 540 \pm 70$ G, $B_1 = 1550 \pm 90$ G, and phase offset $\Phi = 1.67 \pm 0.09$ rad (from the model shown in the top panel of Fig. 11). From the geometrical relations given by Preston (1967, 1974), and with the maximum measured value of $\langle B_z \rangle$ being $\langle B_z \rangle_{\rm max} = 2509 \pm 327$ G, the magnetic axis obliquity angle is then $\beta = 79^{\circ+1}_{-3}$ and the surface magnetic dipole strength is $B_{\rm d} = 11^{+3}_{-1}$ kG (using a linear limb darkening coefficient $\epsilon = 0.4$ from line-blanketed NLTE model spectra; Reeve & Howarth 2016).

Another means of determining W 601 B's ORM parameters is via direct modelling of Stokes V using a version of the Bayesian inference method described by Petit & Wade (2012) modified to include rotational phase information. The results of this fit are shown compared to observations in Fig. 12. Direct modelling of Stokes V produces a best fit for $i_{\rm rot} = 54^{+20}_{-5}$°, $\beta = 60^{+5}_{-10}$°, and $B_{\rm d} = 6.2^{+0.8}_{-0.4}$ kG, where the uncertainties correspond to the 68.7 per cent credible regions. These values differ substantially from the values inferred from $\langle B_z \rangle$ and the stellar parameters, although values of $B_{\rm d}$ comparable to those inferred from $\langle B_z \rangle$ can be accommodated within the 95.4 per cent credible region. Note that, unlike $\langle B_z \rangle$ fitting, direct modelling of the Stokes V profile does not constrain $i_{\rm rot}$ from R_*, $v \sin i$, and $P_{\rm rot}$. The smaller value of $B_{\rm d}$ found by modelling Stokes V is due to the larger value of $i_{\rm rot}$: $i_{\rm rot} < 45°$ is excluded by the Stokes V fits, whereas $i_{\rm rot} > 30°$ is excluded by the star's radius and rotational properties. The Stokes V model and the $\langle B_z \rangle$ model agree well near magnetic maximum at phase 0. However, the $\langle B_z \rangle$ model predicts a crossover signature with a larger amplitude as the magnetic equator comes into view near phases 0.2 and 0.7. A possible reason for this discrepancy may be that, notwithstanding the reasonable fit of a dipole model to $\langle B_z \rangle$, the magnetic field is not purely dipolar but instead a 'distorted dipole' (the most common topology revealed by Zeeman Doppler Imaging; Kochukhov et al. 2019). Supporting this supposition, neither set of ORM parameters provides a faithful reproduction of Stokes V at all phases.

An alternative explanation for the tension between the ORM parameters inferred from $\langle B_z \rangle$ and those obtained via direct modelling of Stokes V is systematic error in W 601 B's stellar parameters. If W 601 B is actually at the ZAMS, then assuming a mass of 5.7 ± 0.3 M$_\odot$ its minimum possible radius is $R_* = 2.9 \pm 0.1$. This results in $i = 44 \pm 3°$, $\beta = 75 \pm 3°$, and $B_{\rm d} = 7.9^{+1}_{-0.7}$ kG, very similar to the values found via modelling of Stokes V. However, this would require $\log g = 4.3$, in which case W 601 A would need to have a surface gravity of 3.7 (left-hand panel of Fig. 6). In this case, the age of the system would need to be about $\log t = 7.2$, which is much older than the NGC 6611 cluster ($\log t \sim 6.75$). W 601 A would also have a much larger radius than W 601 B, which is inconsistent with spectroscopic modelling, which instead indicate their radii are almost identical.

8.1 Magnetic constraints on the primary

The line profiles of the two stellar components are blended in all observations, making it difficult to constrain the magnetic properties of W 601 A. To do this, we subtracted the model fits to Stokes V obtained via Bayesian inference (Fig. 12) from the observed Stokes V profiles, yielding composite LSD profiles consisting of the disentangled Stokes I profiles of W 601 A and the residual Stokes V profiles. We measured FAPs and $\langle B_z \rangle$ in the usual fashion, with an integration range of ± 220 km s^{-1} around the rest frame of W 601 A. All of the profiles are non-detections, indicating that, despite the imperfections in the fit to Stokes V, the residuals are not consistent with statistically significant departures from null polarization. The mean $\langle B_z \rangle$ error bar is 450 G, and the root-mean-square $\langle B_z \rangle$ is 365 G, further confirming that the Zeeman signature was successfully removed.

We then analysed the profiles using the same Bayesian inference engine used to infer ORM parameters for W 601 B, with the difference that, since $P_{\rm rot}$ is unknown, rotational phase was treated as a nuisance parameter (Petit & Wade 2012). The Stokes V profiles yielded upper limits on $B_{\rm d}$ at 68.3 per cent, 95.4 per cent, 99.0 per cent, and 99.7 per cent credible regions of 306 G, 826 G, 1704 G, and 2832 G, respectively. The corresponding upper limits obtained from N are comparable, respectively, 279 G, 779 G, 1590 G, and 2640 G.

Any possible magnetic field possessed by W 601 A is less than W 601 B's by a factor of at least 2 with 99.7 per cent credibility. With

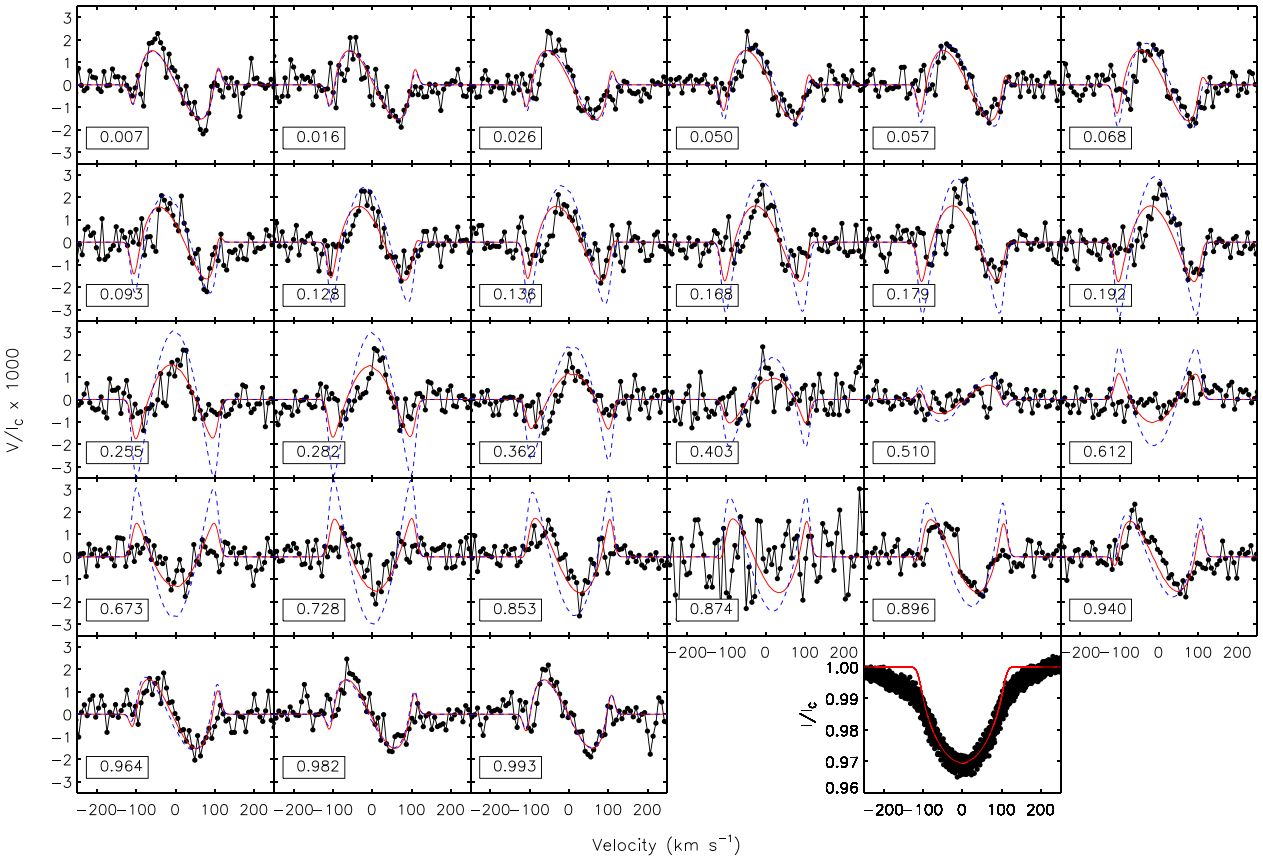

Figure 12. Observed LSD Stokes *V* profiles (black circles) compared to synthetic Stokes *V* profiles inferred from the $\langle B_z \rangle$ curve model (dashed blue) and from direct Bayesian modelling of Stokes *V* (solid red). Rotational phases are indicated in boxes in the upper left corner of each panel. The bottom right panel shows the overplotted disentangled Stokes *I* profiles of W 601 B, as compared to the synthetic Stokes *I* profile (red line) used to model Stokes *V*. Neither model provides a fully satisfactorily reproduction of the Stokes *V* variation.

68.3 per cent credibility its magnetic field is less than 300 G, which is the approximate critical magnetic field strength necessary for the magnetic field to maintain stability against rotational or convective instabilities (Aurière et al. 2007; MacDonald & Petit 2019; Jermyn & Cantiello 2020). Fossil magnetic fields weaker than 300 G are exceptionally uncommon (Aurière et al. 2007; Shultz et al. 2019d; Sikora et al. 2019b), and those magnetic fields that have been detected below this threshold are usually either in evolved stars (e.g. Fossati et al. 2015; Neiner et al. 2017; Martin et al. 2018) or ultraweak fields (of the order of ∼0.1–10 G) as found in Vega (Lignières et al. 2009; Petit et al. 2010), or in Am stars such as Sirius (Petit et al. 2011), Alhena (Blazère, Neiner & Petit 2016; Blazère et al. 2020), and others. While no ultraweak field has yet been detected in a B-type star, the similarly of the magnetic properties of A and B-type stars (Shultz et al. 2019d) suggests that the 'magnetic desert' between the ultraweak fields and fossil magnetic fields likely persists across the entire upper MS. Since the upper limit on W 601 A's magnetic field is comparable to the critical magnetic field strength, any potential magnetic field is likely to be of the order of a few tens of G or less.

9 DISCUSSION

9.1 Magnetosphere

Rapidly rotating, strongly magnetic B-type stars frequently display σ Ori E variability originating in circumstellar magnetospheres (Landstreet & Borra 1978). Hα (Fig. 11, middle) shows a double-wave variation, with the strongest of the maxima corresponding to the $\langle B_z \rangle$ maximum and the weaker local maximum corresponding to the $\langle B_z \rangle$ minimum (vertical lines in Fig. 11). This double-wave EW variation is consistent with line formation within a CM formed in a tilted dipole (Petit et al. 2013). In such a case, the CM is expected to be shaped like a warped disc, with the two densest regions at the intersections of the rotational and magnetic equators (e.g. Townsend & Owocki 2005). When the magnetic pole is closest to the line of sight (i.e. at maximum $|\langle B_z \rangle|$), the projected area of the CM, and therefore the EW of Hα, is at a maximum. If the second magnetic pole is visible at some point during the rotation cycle, this should correspond to a secondary emission peak. This pattern is indeed observed in most CM host stars, the exceptions being those stars with very complex surface magnetic fields (Shultz et al. 2020).

From the star's fundamental and atmospheric parameters, the Vink, de Koter & Lamers (2001) mass-loss recipe yields a mass-loss rate of $\log \dot{M} = -9.5 \pm 0.1$ M$_\odot$ yr^{-1} and a wind terminal velocity of about 1000 km s^{-1}. From equation (7) in ud-Doula & Owocki (2002), the wind magnetic confinement parameter (that is, the ratio of magnetic to kinetic energy density at the magnetic equator at the stellar surface) is $\log \eta_* = 6.0 \pm 0.2$; since η_* is greater than unity the wind is magnetically confined. From equation (9) in ud-Doula et al. (2008), η_* scales to an Alfvén radius (i.e. the maximum extent of magnetic confinement) of $R_A = 32 \pm 4 R_*$.

The Lorentz force enforces corotation of magnetically confined plasma with the stellar magnetic field out to R_A. A CM forms when the Kepler corotation radius R_K, defined as the distance at which

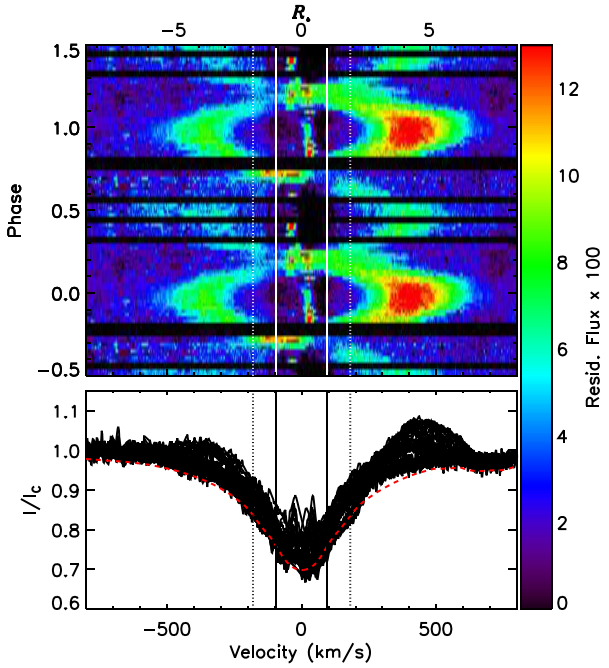

Figure 13. Hα dynamic spectrum. The top panel shows residual flux, shifted to the rest frame of W 601 B, folded with the rotational period, with intensity corresponding to the colour bar. The bottom panel shows the observed spectra (black) and an example synthetic spectrum (red). Residual flux was determined by subtracting synthetic binary spectra tailored to each observation. The vertical solid and dashed lines show $\pm v \sin i = \pm R_*$, and $\pm R_K$, for W 601 B. The asymmetry in emission strength between red and blue emission bumps at phase 0 is likely indicative of a departure from a pure dipole. There is additionally no indication of eclipses in the core of the line.

centrifugal and gravitational forces are balanced, is less than R_A. The Kepler radius is obtained from the critical rotation parameter $W = v_{orb}/v_{eq} = 0.24^{+0.1}_{-0.01}$ via the scaling $R_K/R_* = W^{-2/3}$, where $v_{orb} = \sqrt{GM_*/R_*}$ is the orbital velocity i.e. the velocity required for a Keplerian orbit at the stellar equator (ud-Doula et al. 2008). The equatorial rotational velocity is $v_{eq} = 161^{+32}_{-9}$ km s^{-1}, with a moderate oblateness ratio of the polar to equatorial radii of $R_p/R_e = 0.97 \pm 0.02$. The Kepler corotation radius is then $R_K = 2.1 \pm 0.2\ R_*$ (using equation 14 from ud-Doula et al. 2008). This is a similar Kepler radius to those seen for other Hα-bright CM host stars (Shultz et al. 2019d). R_K is indicated in Fig. 9: as expected, the strongest emission is above the Kepler radius. The ratio of R_A to R_K is $\log(R_A/R_K) = 1.2 \pm 0.1$: not only is R_A significantly greater than R_K, but $\log(R_A/R_K)$ is well within the typical range for Hα-bright CM host stars (Shultz et al. 2019d).

A dynamic spectrum of W 601 B's Hα line is shown in Fig. 13. This was created by subtracting the synthetic spectra used to correct the EWs for the RV variation of the two stars (Section 6, Fig. 9) from the observed spectra, with the residual flux shifted to the rest frame of W 601 B. Due to the rigid rotation of the CM, there is a linear relationship between the projected distance from the star and velocity, i.e. $r/R_* = v_r/v \sin i$ (where v_r is the line-of-sight velocity), as indicated on the top horizontal axis. At maximum emission, there are two emission bumps extending out to several stellar radii, with the strongest emission at about 3.8 R_*. These emission bumps move closer to the line centre as they weaken in strength, corresponding to the reduction of the projected areas of the clouds simultaneous with the reduction in their projected distance from the star. The secondary emission maximum at phase 0.5 has a similar extent in velocity space, but lower peak emission strength, indicating that the CM is more flattened in projection at this phase, which is consistent with the negative pole not coming as close to alignment with the line of sight.

There is stronger emission in the rotationally broadened core of the line around phases 0.25 and 0.75 than is present in this part of the line at other phases. There is nebular emission contaminating the very centre of the line (see also Fig. 9), however, this nebular emission is much narrower than signatures associated with the CM near phases 0.25 and 0.75. There are no enhanced absorption features in the line core at these phases, and therefore no evidence that the star is eclipsed by its CM (as seen for σ Ori, HR 7355, or HD 176582; Bohlender & Monin 2011; Oksala et al. 2012; Rivinius et al. 2013). The presence or absence of eclipses is highly dependent on the magnetic geometry. No eclipses are expected if $i_{rot} \leq 35^\circ$ (Townsend 2008), as inferred from $\langle B_z \rangle$. On the other hand, the ORM parameters inferred from direct modelling of Stokes V predict two prominent eclipses near phase 0.5 (Townsend 2008).

As noted in Section 8, there is some suggestion that W 601 B's surface magnetic field is not purely dipolar. The strong red–blue asymmetry in the Hα emission, especially prominent near phase 0.0 (Fig. 13) can only be explained if the surface magnetic field is not a pure dipole.

Shultz et al. (2020) and Owocki et al. (2020) showed that the peak emission strength of stars with CMs is governed by centrifugal breakout, a magnetic reconnection mechanism whereby the magnetic field is overloaded by the wind-fed plasma and is explosively ejected away from the star (ud-Doula, Townsend & Owocki 2006; ud-Doula et al. 2008). The greater the strength B_K of the magnetic field at the Kepler radius, the greater the density of plasma that the magnetosphere can hold, the more extensive the optically thick part of the Hα-emitting CM, and the stronger the emission. W 601 B's maximum emission strength is about 0.15 nm. W 601 B contributes about 33 per cent of the total light at Hα (as determined from the two stars' radii and synthetic BSTAR2006 spectra for their respective atmospheric parameters), and this emission strength should therefore be scaled up by a factor of about 3, to a single-star emission strength of 0.45 nm. The strength of the equatorial magnetic field at W 601 B's Kepler radius is $\log B_K = 2.7 \pm 0.2$, using the dipole strength inferred from $\langle B_z \rangle$. Utilizing the centrifugal breakout emission strength scaling law developed by Owocki et al. (2020), a star with this value of B_K and W 601 B's stellar and rotational parameters has an expected emission strength of 0.4 ± 0.1 nm, almost exactly the measured value. Notably, this emission strength puts W 601 B in the company of the CM host stars with the strongest Hα emission (namely σ Ori E and HD 345439; Shultz et al. 2020). Using the dipole strength inferred from Stokes V yields $\log B_K = 2.65^{+0.13}_{-0.22}$ and an inferred emission equivalent width of about 0.2 to 0.3 nm, still among the strongest known.

The peak emission strength of W 601 B's CM occurs at about 3.8 R_*, which is about 1.8 R_K. Shultz et al. (2020) noted that R_K is systematically less than the radius of maximum emission, and the discrepancy between the radius of maximum emission and R_K is in this case at the top of the range found for their sample (see their fig. 12). As discussed above in Section 8, the conflict between ORM parameters inferred via modelling of $\langle B_z \rangle$ and via modelling of Stokes V can be reconciled if the radius is smaller than was assumed when deriving ORM parameters from $\langle B_z \rangle$. This smaller radius also yields a larger Kepler radius, $R_K = 2.80 \pm 0.03\ R_*$. This is still only about 70 per cent of the radius of emission maximum, therefore adopting the minimum possible radius cannot resolve the discrepancy in the case of this star.

Binarity is unlikely to have any effect on W 601 B's Hα magnetosphere. The periastron separation of the stars is about 0.9 au (see Tables 2 and 3), whereas the Alfvén radius of W 601 B is a maximum of 37 R_* or, with $R_* = 4.4$ R$_\odot$, about 0.75 au. W 601 A is thus outside of W 601 B's magnetosphere at all orbital phases. This argument is of course sensitive to the mass-loss rate prescription: the much lower Krtička (2014) mass-loss rates imply $R_A = 62^{+22}_{-6}$ R_*, i.e. about $1.3^{+0.4}_{-0.1}$ au, in which case W 601 A is inside the magnetosphere at essentially all orbital phases. In either case, however, W 601 A is very far from the distance of Hα line formation, a maximum of $7R_*$ = 0.15 au from W 601 B.

It is interesting to note that W 601 emits gyrosynchrotron radiation (Kurapati et al. 2017), which is believed to be generated by electrons accelerated to relativistic energies within the middle magnetosphere current sheet just outside the Alfvén radius (Trigilio et al. 2004). If W 601 B's current sheet extends far enough beyond R_A (which is by no means excluded by the models developed by Trigilio et al. 2004), it may be possible that W 601 A disrupts the current sheet during periastron passage. It would be of interest to obtain radio observations of this system at apastron and periastron, in order to look for such an effect.

9.2 Rotational and magnetic evolution

Among the magnetic high-mass PMS stars, W 601 B has both the strongest magnetic field and one of the shortest rotation periods. Of the magnetic PMS stars noted in the introduction, the mean surface dipole strength is about 1.2 kG, and the strongest belongs to V 380 Ori (with a strength of 2.2 kG; Alecian et al. 2009), while the measured rotation periods of other magnetic PMS hot stars range from 4 to 40 d (Alecian et al. 2009; Järvinen et al. 2015). This makes W 601 B's rotational and magnetic evolution of some interest.

MS magnetic hot stars experience simultaneous decline in surface magnetic field strength, due to a combination of magnetic flux conservation in an expanding atmosphere and magnetic flux decay, and rapid magnetic braking due to angular momentum loss (ud-Doula et al. 2008; Shultz et al. 2019d). As a PMS star, W 601 B is still contracting towards the ZAMS. Therefore, flux conservation would imply that its surface magnetic field should grow stronger as the radius shrinks, while at the same time conservation of angular momentum would normally mean that the star should spin-up. In this case, the current radius of about 4.4 R$_\odot$ should shrink to about 3.2 R$_\odot$ at the ZAMS. The total unsigned magnetic flux is $\Phi = B_d R_*^2$, therefore if flux is conserved then the ZAMS field should increase to about 21^{+5}_{-2} kG. This is comparable to the top of the range of surface magnetic dipole strengths of magnetic early B-type stars seen close to the ZAMS (Shultz et al. 2019d).

At the same time, conservation of angular momentum means that the star should spin-up as it approaches the ZAMS. Under the assumption that angular momentum is conserved, the ZAMS equatorial rotational velocity should be $v_{eq,ZAMS} = v_{eq} R_*/R_{ZAMS} = 250^{+46}_{-15}$ km s^{-1}, corresponding to a rotational period $P_{rot,ZAMS} \sim 0.7$ d. This is similar to the two most rapidly rotating magnetic B-type stars known, HR 5907 and HR 7355 (Grunhut et al. 2012; Rivinius et al. 2013), which have periods of about 0.5 d.

Angular momentum of course should not be conserved, since it is being lost via the magnetosphere. From equation (20) in ud-Doula, Owocki & Townsend (2009), the spin-down time-scale τ_J – i.e. the e-folding time-scale for the rotation parameter W – is $\log(\tau_J/\mathrm{yr}) = 5.9^{+0.3}_{-0.1}$ or between 700 kyr and 1.5 Myr, using the Vink et al. (2001) mass-loss rates. If Krtička (2014) mass-loss rates are used instead, $\log(\tau_J/\mathrm{yr}) = 6.5^{+0.3}_{-0.1}$. Given the current age of the star, it should reach the ZAMS in about 300 kyr, i.e. about half an e-folding time-scale using Vink mass-loss, and much shorter than τ_J using Krtička mass-loss. As the star evolves towards the ZAMS, its rotational evolution should therefore be dominated by spin-up due to contraction.

We conducted an analysis of the rotational evolution of W 601 B using the 7 M$_\odot$ PMS Haemmerlé et al. (2019) evolutionary track, simultaneously accounting for angular momentum loss via the magnetosphere, spin-up due to contraction towards the ZAMS, and the change in B_d due to flux conservation. The model had an initial dipole strength $B_{d,init} = 11$ kG. We started the model at 4 R$_\odot$ (corresponding to an age of 400 kyr from the birthline), with $W = 0.3$ (corresponding to $P_{rot} \sim 1.13$ d). The minimum rotation period in this case is achieved at 490 kyr, with $P_{rot} \sim 0.55$ d; after this point magnetic braking dominates the rotational evolution. This corresponds to a spin-up of -0.5 s yr^{-1}. More accurate predictions of the spin-up rate may be provided by the development of a PMS extension of self-consistent stellar evolutionary models incorporating fossil fields, similar to those presented by Keszthelyi et al. (2020).

Rotational evolution has been detected in several magnetic early-type stars. σ Ori E is spinning down at a rate of about $+0.08$ s yr^{-1}, consistent with expectations from magnetic braking (Townsend et al. 2010). HD 37776 and CU Vir both exhibit complex patterns of cyclical spin-up and spin-down (Mikulášek et al. 2008, 2011, 2017), with typical period changes of the order of 0.6 s yr^{-1} and 0.1 s yr^{-1}, respectively. HD 142990 is spinning up at a rate of about -0.6 s yr^{-1} (Shultz et al. 2019c). It is intriguing to note that both HD 37776 and HD 142990 are very young stars (Shultz et al. 2019d), and their spin-up rates are comparable to that expected for W 601 B. While contraction towards the ZAMS cannot explain the cyclical nature of HD 37776's period evolution, it may provide an explanation for that of HD 142990. In all cases in which rotational evolution has been directly measured, the data sets have spanned about 30 yr; it is therefore not yet possible to detect rotational evolution in W 601 B, since the data set for this star extends across only 7 yr, with the majority of the data having been acquired over a 2-yr time span.

Shultz et al. (2019d) noted that ultraslow rotators such as ξ^1 CMa (Shultz et al. 2017, 2018c) are difficult to explain using standard magnetic braking theory. In particular, they are so slowly rotating that their rotation periods are even longer than can be explained by standard magnetic braking theory under the usual assumption of initially critical rotation (ud-Doula et al. 2009; Petit et al. 2013). One possible explanation is that such stars lose a great deal of angular momentum on the PMS. Indeed, their initial critical rotation fraction at the ZAMS would need to already be very close to 0. So far no such magnetic PMS B-type stars have been found (although the magnetic Herbig Ae star HD 101412 is quite a slow rotator, with a period of 42 d; Järvinen et al. 2015). Instead, W 601 B is apparently a precursor of stars that arrive at the ZAMS as rapid rotators. However, at this point relatively few magnetic PMS hot stars are known; identifying a larger sample is crucial to determining whether there is indeed a sub-population of PMS slow rotators that can serve as the progenitors for stars such as ξ^1 CMa, or whether some additional braking mechanism is necessary to explain ultraslow rotation.

9.3 Implications for the origin of fossil magnetic fields

Using the same 7 M$_\odot$ evolutionary track, once again assuming magnetic flux conservation and evolving back in time from W 601 B's current magnetic parameters, its surface magnetic dipole would have been at a minimum intensity of about 700 G approximately 140 kyr ago. Assuming the same i_{rot} and β as presently, $B_d = 700$ G would

yield a maximum $\langle B_z \rangle$ of about 130 G. This is comparable to the typical $\langle B_z \rangle$ values observed by Villebrun et al. (2019) in their study of T-Tauri Stars (TTSs), Intermediate Mass T-Tauri Stars (IMTTSs), and Herbig Ae stars.

This surface dipole strength is also comparable to the mean surface magnetic field strengths of TTSs and IMTTSs, which range from a few hundred G to a few kG (Donati et al. 2007, 2008, 2010, 2011a, b, 2013, 2015; Hussain et al. 2009; Johns-Krull et al. 2013; Kochukhov 2015; Hill et al. 2017; Lavail et al. 2017, 2020; Yu et al. 2017). The continuity in total unsigned magnetic flux between stars at various stages on the PMS and MS, and across a wide range of masses, is suggestive of a common origin of fossil magnetic fields in dynamo processes occurring early in the evolutionary process. A striking property of several studies of magnetic binaries is that the magnetic properties of the two stars are often remarkably different even when their masses and rotational properties are nearly identical. For stars with convective envelopes, this manifests as one star having a globally organized poloidal field and the other a more tangled magnetic topology. This is so for both V1878 Ori, and the MS M dwarf visual binary GJ65 A and B (Kochukhov & Lavail 2017). In the case of the B9 V 'identical twin' eclipsing binary HD 62658, one of the two stars is a chemically peculiar Bp star with a strong magnetic field, while the other is a normal, non-magnetic B-type star (Shultz et al. 2019e). Another example is provided by the B2 IV binary HD 149277, with a mass ratio of 1.1, in which one component is a He-strong star with a surface dipole strength of several kG, and the other has no detectable magnetic field (Shultz 2016; González et al. 2018). While the mass ratio of W 601 is much larger than these systems, it follows the general pattern of one component hosting a very strong magnetic field, while the upper limit for the magnetic field of the other is comparable to the 300 G critical field strength and therefore probably of the order of a few G (Section 8.1), and confirms that this pattern is established already on the PMS.

The existence of several close binaries containing a magnetic star poses a challenge to the scenario in which dynamos generated during binary mergers are the primary pathway to fossil magnetic fields (e.g. Schneider et al. 2019), since mergers should not produce close binaries. Shultz et al. (2019e) suggested that the properties of the binaries above point to an alternative scenario. During the convective stage of the star's evolution, irrespective of rotational properties or stellar mass, the dynamo magnetic field spontaneously settles into one of two attractor states: a globally organized dipole, or a tangled topology. Both leave behind a fossil field when the star becomes fully radiative. However, weaker or more tangled fields rapidly decay under the influence of rotational or convective instabilities (e.g. Aurière et al. 2007; MacDonald & Petit 2019; Jermyn & Cantiello 2020). In the case of close binaries, flux decay is accelerated via tidally induced instabilities (Vidal et al. 2019). The result is that, very shortly after the cessation of convective support for a dynamo, only the strongest and most organized magnetic fields survive, while the incidence of magnetic fields among close binary stars is decreased even further by the additional influence of tidal instabilities. The abrupt change in magnetic incidence from essentially 100 per cent to the canonical 10 per cent seen for MS hot stars is precisely what is seen at the boundary between stars with convective envelopes and fully radiative stars (Villebrun et al. 2019).

9.4 Formation of surface chemical abundance peculiarities

The existence of He spots on the surface of W 601 B, as inferred from the rotational modulation of the He I 667.8 nm line (Fig. 11), indicates that surface chemical abundances become established quite rapidly on the PMS following the formation of the radiative envelope. It is instructive in this regard to compare W 601 B with other magnetic hot stars on the PMS. HD 72106 A (B9p) is the magnetic primary of a PMS SB2 system, with a non-magnetic Herbig Ae companion (Folsom et al. 2008). The primary, which either is just reaching or has just passed the ZAMS, already possesses strong chemical peculiarities, while the non-magnetic companion has normal chemical abundances. This is similar to the case of W 601. By contrast, the magnetic Herbig Ae star HD 190073 has normal chemical abundances (Catala et al. 2007; Folsom et al. 2012), while another magnetic Herbig Ae star, HD 101412 (Wade et al. 2005; Hubrig et al. 2009), is underabundant in some elements (Cowley et al. 2010; Folsom et al. 2012). The abundances of HD 101412 appear to reflect those of its dust-depleted accreting material (Kama, Folsom & Pinilla 2015).

Notably, both HD 190073 and HD 101412 possess emission lines, which are most likely formed in accretion discs. HD 72106 A does not show Herbig emission, and while W 601 B is an Hα-bright star its emission originates in a CM and not an accretion disc. The scenario that emerges from this comparison is one in which magnetic hot stars that are still accreting possess surface abundances reflecting the accreting material. Once accretion ceases, diffusion in the magnetically stabilized radiative envelope leads to the rapid emergence of surface chemical peculiarities. Another interesting point of comparison is the PMS Am star Stock 16 12 (Netopil et al. 2014). While Am stars do not possess strong magnetic fields, the existence of chemical peculiarities on a non-accreting PMS star is further evidence that these can form rapidly once accretion has ceased.

The secondary of this system is a chemically normal A-type star, which is much closer to the birthline, and it is possible that the Herbig emission originates from this component (as also suggested by Hubrig et al. 2019, who noted a lack of periodicity in the circumstellar emission lines). However, a detailed analysis by Alecian et al. (2009) of RVs, spectroscopic emission, and SEDs obtained from speckle interferometric data (Leinert, Richichi & Haas 1997) demonstrated that the emission does not originate around the tertiary, and most likely belongs either to the primary or to a circumbinary accretion disc.

Atomic diffusion in PMS stars was evaluated by Vick et al. (2011) in order to determine how quickly the Ap/Bp phenomenon can be established. They found that, so long as turbulence is suppressed, surface chemical abundance peculiarities can form within 20 to 2 Myr, with the time-scale decreasing with increasing stellar mass. While the minimum time-scale is significantly longer than the PMS lifetime of W 601 B, the models utilized by Vick et al. (2011) extended only up to 2.8 $M_\odot$, much lower than W 601 B's mass. Although models of higher mass PMS stars are needed to explore the parameter space occupied by W 601 B, the trend of decreasing time-scales with increasing mass suggests that the formation of chemical spots on W 601 B's surface within a few hundred kyr is probably not in conflict with our current understanding. It is worth noting that suppression of turbulence within subsurface opacity-bump convection zones is both expected (MacDonald & Petit 2019; Jermyn & Cantiello 2020) and observed (Sundqvist et al. 2013) in strongly magnetic early-type stars, and that the criterion that turbulence be suppressed is therefore very likely to be fulfilled.

10 CONCLUSIONS

We have analysed a large spectropolarimetric data set of the magnetic PMS star W 601. The system turns out to be a spectroscopic binary

with a mass ratio of 1.8 and an orbital period of about 110 d. Atmospheric parameters ($T_{\rm eff}$ and $\log g$) were determined for the two stars via spectroscopic analysis. The $T_{\rm eff}$ of the primary, W 601 A, is about 22 kK, consistent with previous determinations for this star; the secondary, W 601 B, is slightly cooler at about 19 kK. W 601 A has a mass of about 12 $M_\odot$, and W 601 B has a mass of about 7 $M_\odot$.

Magnetic analysis reveals that the magnetic field belongs to W 601 B. The peak $\langle B_z \rangle$ measured from disentangled LSD profiles is about 2 kG.

W 601 was originally classified as a Herbig Be star by Alecian et al. (2008b) due to its Hα emission and mid-infrared excess. However, close examination of Hα shows that it varies coherently with $\langle B_z \rangle$, and displays the typical features of a CM. W 601 is therefore not a classical Herbig Be star. However, both components have low surface gravities, around 3.8. Such a low $\log g$ indicates that the two stars are either very evolved (around 22 Myr old) or still contracting towards the MS. Only the latter hypothesis is consistent with W 601's membership in the NGC 6611 open cluster, which has an MS turnoff age of 2–4 Myr reflecting the oldest populations in the cluster, but also contains ongoing star formation. Even if W 601 is not a member of the cluster, if the stars are on the MS the low $\log g$ implies that W 601 A must be near the TAMS; given the mass ratio, W 601 B should still be near the ZAMS and have a much higher surface gravity than is consistent with the data. Spectroscopic modelling furthermore indicates that the two stars have similar radii, which again is only possible if they are still on the PMS. Therefore, while W 601 is not a classical Herbig Be star, the orbital and spectroscopic properties of the system indicate that it is probably a PMS star as suggested by Martayan et al. (2008) and Alecian et al. (2008b).

A rotational period of about 1.13 d was determined from Hα and $\langle B_z \rangle$. Modelling of $\langle B_z \rangle$ using this period and W 601 B's stellar parameters yields $B_{\rm d} \sim 11$ kG. This makes W 601 B by far the most strongly magnetic of the known magnetic PMS stars. When the magnetic star's emission strength is corrected for dilution by the non-magnetic primary, W 601 B is also revealed to have Hα emission comparable to the strongest seen in the population of CM host stars. This extremely strong emission is consistent with the star's rapid rotation, strong surface magnetic field, mass, and radius. Indeed, the star's emission strength is very close to the value predicted by both empirical (Shultz et al. 2020) and theoretical (Owocki et al. 2020) analyses of similar stars based on the centrifugal breakout mass balancing mechanism.

While $\langle B_z \rangle$ is consistent with a tilted dipole, Stokes V is not satisfactorily reproduced by a purely dipolar model. Strong red–blue asymmetry in the Hα emission is furthermore indicative that the surface magnetic field is not purely dipolar. This indicates that distortions to the magnetic dipole are already present on the PMS.

W 601 B is a He-strong star with weakly variable He lines, indicating that surface chemical abundance peculiarities are also already established on the PMS. We were unable to detect indications of significant departure from solar abundances in other spectroscopic lines, or statistically significant variability in the stronger metallic lines. This may indicate that the star is still in the process of forming its surface chemical abundance spots, and that so far only the He spots have become noticeable. On the other hand, the low S/N of the data may simply make metallic abundance patches difficult to detect.

Extrapolation of W 601 B's magnetic and rotational properties as it contracts towards the ZAMS indicates that it should arrive on the MS with a surface dipole magnetic field strength of about 20 kG and a rotational period of about 0.6 d. Thus, when W 601 B arrives on the MS, it will have among the most extreme magnetic and rotational properties of any known magnetic hot star. W 601 B is therefore a precursor to objects such as σ Ori E, HR 5907, or HR 7355. The expected rate of rotational spin-up, about -0.5 s yr^{-1}, is similar to the rate recently determined by Shultz et al. (2019c) for HD 142990 and is in principle detectable if the star is monitored over the next 10 or 20 yr.

ACKNOWLEDGEMENTS

The authors acknowledge the numerous helpful comments made by the referee, Dr Gregory Herczeg, which have greatly improved the quality of this paper. This work is based on observations obtained at the Canada–France–Hawaii Telescope (CFHT) that is operated by the National Research Council of Canada, the Institut National des Sciences de l'Univers (INSU) of the Centre National de la Recherche Scientifique (CNRS) of France, and the University of Hawaii. The MiMeS Collaboration acknowledges financial support from the Programme National de Physique Stellaire (PNPS) of INSU/CNRS. MES acknowledges financial support from the Annie Jump Cannon Fellowship, supported by the University of Delaware and endowed by the Mount Cuba Astronomical Observatory. EA acknowledges financial support from 'Programme National de Physique Stellaire' (PNPS) of CNRS/INSU (France). VP acknowledges support from the National Science Foundation under Grant No. 1747658. GAW acknowledges support from the Natural Sciences and Engineering Research Council (NSERC) of Canada in the form of a Discovery Grant.

DATA AVAILABILITY

Reduced ESPaDOnS spectra are available at the CFHT archive maintained by the CADC at https://www.cadc-ccda.hia-iha.nrc-cnrc.gc.ca/en/, where they can be found via standard stellar designations.

REFERENCES

Alecian E. et al., 2008a, MNRAS, 385, 391
Alecian E. et al., 2008b, A&A, 481, L99
Alecian E. et al., 2009, MNRAS, 400, 354
Alecian E. et al., 2013a, MNRAS, 429, 1001
Alecian E., Wade G. A., Catala C., Grunhut J. H., Landstreet J. D., Böhm T., Folsom C. P., Marsden S., 2013b, MNRAS, 429, 1027
Aurière M. et al., 2007, A&A, 475, 1053
Bagnulo S., Landstreet J. D., Fossati L., Kochukhov O., 2012, A&A, 538, A129
Blazère A., Neiner C., Petit P., 2016, MNRAS, 459, L81
Blazère A., Petit P., Neiner C., Folsom C., Kochukhov O., Mathis S., Deal M., Landstreet J., 2020, MNRAS, 492, 5794
Bloomfield P., 1976, Fourier Analysis of Time Series: An Introduction. Wiley, New York
Bohlender D. A., Monin D., 2011, AJ, 141, 169
Bonnell I. A., Bate M. R., 1994, MNRAS, 271, 999
Bouvier J. et al., 2007, A&A, 463, 1017
Braithwaite J., Spruit H. C., 2004, Nature, 431, 819
Breger M. et al., 1993, A&A, 271, 482
Cantat-Gaudin T. et al., 2018, A&A, 618, A93
Catala C. et al., 2007, A&A, 462, 293
Cowley C. R., Hubrig S., González J. F., Savanov I., 2010, A&A, 523, A65
Cutri R. M. et al., 2003, VizieR Online Data Catalog, 2246, 0
de Winter D., Koulis C., The P. S., van den Ancker M. E., Perez M. R., Bibo E. A., 1997, A&AS, 121, 223
Donati J.-F., Semel M., Rees D. E., 1992, A&A, 265, 669
Donati J.-F., Semel M., Carter B. D., Rees D. E., Collier Cameron A., 1997, MNRAS, 291, 658
Donati J. F. et al., 2007, MNRAS, 380, 1297

Donati J. F. et al., 2008, MNRAS, 386, 1234
Donati J. F. et al., 2010, MNRAS, 409, 1347
Donati J. F. et al., 2011a, MNRAS, 417, 472
Donati J. F. et al., 2011b, MNRAS, 417, 1747
Donati J. F. et al., 2013, MNRAS, 436, 881
Donati J. F. et al., 2015, MNRAS, 453, 3706
Dufton P. L. et al., 2006, A&A, 457, 265
Ekström S. et al., 2012, A&A, 537, A146
Evans C. J. et al., 2005, A&A, 437, 467
Fitzpatrick E. L., Massa D., 1999, ApJ, 525, 1011
Folsom C. P., Wade G. A., Kochukhov O., Alecian E., Catala C., Bagnulo S., Landstreet J. D., Hanes D., 2008, Contrib. Astron. Obs. Skalnate Pleso, 38, 245
Folsom C. P., Bagnulo S., Wade G. A., Alecian E., Landstreet J. D., Marsden S. C., Waite I. A., 2012, MNRAS, 422, 2072
Folsom C. P., Likuski K., Wade G. A., Kochukhov O., Alecian E., Shulyak D., 2013, MNRAS, 431, 1513
Fossati L. et al., 2015, A&A, 574, A20
Gaia Collaboration, 2018, A&A, 616, A1
Getman K. V., Feigelson E. D., Kuhn M. A., Bate M. R., Broos P. S., Garmire G. P., 2018, MNRAS, 476, 1213
González J. F., Levato H., 2006, A&A, 448, 283
González J. F., Hubrig S., Järvinen S. P., Schöller M., 2018, MNRAS, 481, L30
Grunhut J. H. et al., 2012, MNRAS, 419, 1610
Grunhut J. H. et al., 2017, MNRAS, 465, 2432
Guarcello M. G., Prisinzano L., Micela G., Damiani F., Peres G., Sciortino S., 2007, A&A, 462, 245
Haemmerlé L. et al., 2019, A&A, 624, A137
Hill C. A., Carmona A., Donati J. F., Hussain G. A. J., Gregory S. G., Alencar S. H. P., Bouvier J., Matysse Collaboration, 2017, MNRAS, 472, 1716
Hillenbrand L. A., Massey P., Strom S. E., Merrill K. M., 1993, AJ, 106, 1906
Horne J. H., Baliunas S. L., 1986, ApJ, 302, 757
Hubrig S. et al., 2009, A&A, 502, 283
Hubrig S., Ilyin I., Schöller M., Lo Curto G., 2013, Astron. Nachr., 334, 1093
Hubrig S., Carroll T. A., Scholler M., Ilyin I., 2015, MNRAS, 449, L118
Hubrig S., Järvinen S. P., Schöller M., Carroll T. A., Ilyin I., Pogodin M. A., 2019, in Kudryavtsev D. O., Romanyuk I. I., Yakunin I. A., eds, ASP Conf. Ser. Vol. 518, Physics of Magnetic Stars. Astron. Soc. Pac., San Francisco, p. 18
Hussain G. A. J. et al., 2009, MNRAS, 398, 189
Høg E. et al., 2000, A&A, 355, L27
Järvinen S. P., Carroll T. A., Hubrig S., Schöller M., Ilyin I., Korhonen H., Pogodin M., Drake N. A., 2015, A&A, 584, A15
Jermyn A. S., Cantiello M., 2020, ApJ, 900, 113
Johns-Krull C. M. et al., 2013, ApJ, 765, 11
Kama M., Folsom C. P., Pinilla P., 2015, A&A, 582, L10
Keszthelyi Z. et al., 2020, MNRAS, 493, 518
Kochukhov O., 2015, A&A, 580, A39
Kochukhov O., Lavail A., 2017, ApJ, 835, L4
Kochukhov O., Makaganiuk V., Piskunov N., 2010, A&A, 524, A5
Kochukhov O. et al., 2015, A&A, 574, A79
Kochukhov O., Shultz M., Neiner C., 2019, A&A, 621, A47
Krtička J., 2014, A&A, 564, A70
Kuhn M. A., Hillenbrand L. A., Sills A., Feigelson E. D., Getman K. V., 2019, ApJ, 870, 32
Kumar B., Sagar R., Sanwal B. B., Bessell M. S., 2004, MNRAS, 353, 991
Kupka F. G., Piskunov N., Ryabchikova T. A., Stempels H. C., Weiss W. W., 1999, A&AS, 138, 119
Kupka F. G., Ryabchikova T. A., Piskunov N. E., Stempels H. C., Weiss W. W., 2000, Balt. Astron., 9, 590
Kurapati S. et al., 2017, MNRAS, 465, 2160
Kuschnig R., Weiss W. W., Gruber R., Bely P. Y., Jenkner H., 1997, A&A, 328, 544
Landstreet J. D., Borra E. F., 1978, ApJ, 224, L5
Landstreet J. D., Bagnulo S., Andretta V., Fossati L., Mason E., Silaj J., Wade G. A., 2007, A&A, 470, 685
Landstreet J. D. et al., 2008, A&A, 481, 465
Lanz T., Hubeny I., 2007, ApJS, 169, 83
Lavail A., Kochukhov O., Hussain G. A. J., Alecian E., Herczeg G. J., Johns-Krull C., 2017, A&A, 608, A77
Lavail A., Kochukhov O., Hussain G. A. J., Argiroffi C., Alecian E., Morin J., BinaMIcS Collaboration, 2020, MNRAS, 497, 632
Leinert C., Richichi A., Haas M., 1997, A&A, 318, 472
Lenz P., Breger M., 2005, Commun. Asteroseismology, 146, 53
Lignières F., Petit P., Böhm T., Aurière M., 2009, A&A, 500, L41
MacDonald J., Petit V., 2019, MNRAS, 487, 3904
Maíz Apellániz J., Barbá R. H., 2018, A&A, 613, A9
Martayan C., Floquet M., Hubert A. M., Neiner C., Frémat Y., Baade D., Fabregat J., 2008, A&A, 489, 459
Martin A. J. et al., 2018, MNRAS, 475, 1521
Mathys G., 1989, Fundam. Cosm. Phys., 13, 143
Mendigutía I., Eiroa C., Montesinos B., Mora A., Oudmaijer R. D., Merín B., Meeus G., 2011a, A&A, 529, A34
Mendigutía I., Calvet N., Montesinos B., Mora A., Muzerolle J., Eiroa C., Oudmaijer R. D., Merín B., 2011b, A&A, 535, A99
Mestel L., 1999, Stellar Magnetism. Clarendon, Oxford, p. 99
Mikulášek Z. et al., 2008, A&A, 485, 585
Mikulášek Z. et al., 2011, A&A, 534, L5
Mikulášek Z. Z., Krtička J., Janík J., Henry G. W., Zejda M., Shultz M., Paunzen E., Jagelka M., 2017, in Balega Y. Y., Kudryavtsev D. O., Romanyuk I. I., Yakunin I. A., eds, ASP Conf. Ser. Vol. 510, Stars: From Collapse to Collapse. Astron. Soc. Pac., San Francisco, p. 220
Nazé Y., Petit V., Rinbrand M., Cohen D., Owocki S., ud-Doula A., Wade G. A., 2014, ApJS, 215, 10
Neiner C., Mathis S., Alecian E., Emeriau C., Grunhut J., BinaMIcS, MiMeS Collaborations, 2015, in Nagendra K. N., Bagnulo S., Centeno R., Jesús Martínez González M., eds, Proc. IAU Symp. 305, Polarimetry, Cambridge University Press.p. 61
Neiner C. et al., 2017, MNRAS, 471, 1926
Netopil M., Fossati L., Paunzen E., Zwintz K., Pintado O. I., Bagnulo S., 2014, MNRAS, 442, 3761
Nieva M.-F., 2013, A&A, 550, A26
Oksala M. E., Wade G. A., Townsend R. H. D., Owocki S. P., Kochukhov O., Neiner C., Alecian E., Grunhut J., 2012, MNRAS, 419, 959
Owocki S. P., Shultz M. E., ud-Doula A., Sundqvist J. O., Townsend R. H. D., Cranmer S. R., 2020, MNRAS, 499, 5366
Pablo H. et al., 2019, MNRAS, 488, 64
Pecaut M. J., Mamajek E. E., 2013, ApJS, 208, 9
Petit V., Wade G. A., 2012, MNRAS, 420, 773
Petit V., Wade G. A., Drissen L., Montmerle T., Alecian E., 2008, MNRAS, 387, L23
Petit P. et al., 2010, A&A, 523, A41
Petit P. et al., 2011, A&A, 532, L13
Petit V. et al., 2013, MNRAS, 429, 398
Petit V. et al., 2019, MNRAS, 489, 5669
Piskunov N. E., Kupka F., Ryabchikova T. A., Weiss W. W., Jeffery C. S., 1995, A&AS, 112, 525
Preston G. W., 1967, ApJ, 150, 547
Preston G. W., 1974, ARA&A, 12, 257
Reeve D. C., Howarth I. D., 2016, MNRAS, 456, 1294
Rivinius T., Townsend R. H. D., Kochukhov O., Štefl S., Baade D., Barrera L., Szeifert T., 2013, MNRAS, 429, 177
Rusomarov N., Kochukhov O., Ryabchikova T., Piskunov N., 2015, A&A, 573, A123
Rusomarov N., Kochukhov O., Ryabchikova T., Ilyin I., 2016, A&A, 588, A138
Rusomarov N., Kochukhov O., Lundin A., 2018, A&A, 609, A88
Ryabchikova T. A., Piskunov N. E., Kupka F., Weiss W. W., 1997, Balt. Astron., 6, 244
Ryabchikova T., Piskunov N., Kurucz R. L., Stempels H. C., Heiter U., Pakhomov Y., Barklem P. S., 2015, Phys. Scr., 90, 054005
Schneider F. R. N., Ohlmann S. T., Podsiadlowski P., Röpke F. K., Balbus S. A., Pakmor R., Springel V., 2019, Nature, 574, 211
Schöller M. et al., 2016, A&A, 592, A50
Shultz M., 2016, PhD thesis, Queen's University

Shultz M. et al., 2015a, MNRAS, 449, 3945
Shultz M., Wade G. A., Alecian E., BinaMIcS Collaboration, 2015b, MNRAS, 454, L1
Shultz M., Wade G. A., Rivinius T., Neiner C., Henrichs H., Marcolino W., MiMeS Collaboration, 2017, MNRAS, 471, 2286
Shultz M., Rivinius T., Wade G. A., Alecian E., Petit V., 2018a, MNRAS, 475, 839
Shultz M. E. et al., 2018b, MNRAS, 475, 5144
Shultz M., Kochukhov O., Wade G. A., Rivinius T., 2018c, MNRAS, 478, L39
Shultz M. et al., 2019a, MNRAS, 482, 3950
Shultz M. E. et al., 2019b, MNRAS, 485, 1508
Shultz M., Rivinius T., Das B., Wade G. A., Chand ra P., 2019c, MNRAS, 486, 5558
Shultz M. E. et al., 2019d, MNRAS, 490, 274
Shultz M. E. et al., 2019e, MNRAS, 490, 4154
Shultz M. E. et al., 2020, MNRAS, 499, 5379
Sikora J., Wade G. A., Power J., Neiner C., 2019a, MNRAS, 483, 2300
Sikora J., Wade G. A., Power J., Neiner C., 2019b, MNRAS, 483, 3127
Silvester J., Kochukhov O., Rusomarov N., Wade G. A., 2017, MNRAS, 471, 962
Stibbs D. W. N., 1950, MNRAS, 110, 395
Sundqvist J. O., Petit V., Owocki S. P., Wade G. A., Puls J., MiMeS Collaboration, 2013, MNRAS, 433, 2497
Townsend R. H. D., 2008, MNRAS, 389, 559
Townsend R. H. D., Owocki S. P., 2005, MNRAS, 357, 251
Townsend R. H. D., Oksala M. E., Cohen D. H., Owocki S. P., ud-Doula A., 2010, ApJ, 714, L318
Trigilio C., Leto P., Umana G., Leone F., Buemi C. S., 2004, A&A, 418, 593
ud-Doula A., Owocki S. P., 2002, ApJ, 576, 413
ud-Doula A., Townsend R. H. D., Owocki S. P., 2006, ApJ, 640, L191
ud-Doula A., Owocki S. P., Townsend R. H. D., 2008, MNRAS, 385, 97
ud-Doula A., Owocki S. P., Townsend R. H. D., 2009, MNRAS, 392, 1022
Vick M., Michaud G., Richer J., Richard O., 2011, A&A, 526, A37
Vidal J., Cébron D., ud-Doula A., Alecian E., 2019, A&A, 629, A142
Villebrun F. et al., 2019, A&A, 622, A72
Vink J. S., de Koter A., Lamers H. J. G. L. M., 2001, A&A, 369, 574
Vink J. S., Drew J. E., Harries T. J., Oudmaijer R. D., Unruh Y., 2005, MNRAS, 359, 1049
Wade G. A., Donati J.-F., Landstreet J. D., Shorlin S. L. S., 2000, MNRAS, 313, 851
Wade G. A. et al., 2005, A&A, 442, L31
Wade G. A. et al., 2016, MNRAS, 456, 2
Wichittanakom C., Oudmaijer R. D., Fairlamb J. R., Mendigutía I., Vioque M., Ababakr K. M., 2020, MNRAS, 493, 234
Wolff S. C., Strom S. E., Dror D., Venn K., 2007, AJ, 133, 1092
Yu L. et al., 2017, MNRAS, 467, 1342

This paper has been typeset from a TEX/LATEX file prepared by the author.